Growth of continental crust and subduction of lithosphere in the Hadean revealed by geochemistry and geodynamics.

Alexander V Sobolev, Adrien Vezinet, Aleksandr V Chugunov, Charitra Jain, Stephan V Sobolev, Evgeny V Asafov, Valentina G Batanova, Nicholas T Arndt, Leonid V Danyushevsky, John W Valley, et al.

Growth of continental crust and subduction of lithosphere in the Hadean revealed by geochemistry and geodynamics.

Alexander Sobolev

alexander.sobolev@univ-grenoble-alpes.fr

University Grenoble Alpes https://orcid.org/0000-0002-1997-2032

Adrien Vezinet

University Grenoble Alpes https://orcid.org/0000-0001-9975-2760

Aleksandr Chugunov

University Grenoble Alpes

Charitra Jain

GFZ German Research Centre for Geosciences https://orcid.org/0000-0002-0562-2568

Stephan Sobolev

GFZ-Potsdam

Evgeny Asafov

Vernadsky Institute of Geochemistry and Analytical Chemistry, Russian Academy of Sciences

Valentina Batanova

ISTerre

Nicholas Arndt

University Grenoble Alpes

Leonid Danyushevsky

Norris Scientific

John Valley

University of Wisconsin, Madison

Alina Koshlykova

Vernadsky Institute of Geochemistry and Analytical Chemistry, Russian Academy of Science

Article

Keywords:

Posted Date: November 1st, 2024

DOI: https://doi.org/10.21203/rs.3.rs-3601806/v1

Additional Declarations: There is **NO** Competing Interest.

Growth of continental crust and subduction of lithosphere in the Hadean revealed by geochemistry and geodynamics

Adrien Vezinet[1]*†, Aleksandr V. Chugunov[1]*†, Alexander V. Sobolev[1]*†, Charitra Jain[2], Stephan V. Sobolev[2,3]*, Valentina G. Batanova[1], Evgeny V. Asafov[4], Alina N. Koshlyakova[4], Nicholas T. Arndt[1], Leonid V. Danyushevsky[5], and John W. Valley[6]

Affiliations:

[1] Univ. Grenoble Alpes, Univ. Savoie Mont Blanc, CNRS, IRD, Univ. Gustave Eiffel, ISTerre; 38000 Grenoble, France.

[2] GFZ German Research Centre for Geosciences, Geodynamic Modeling Section; Potsdam, Germany.

[3] University of Potsdam, Institute of Geosciences; Potsdam, Germany.

[4] Vernadsky Institute of Geochemistry and Analytical Chemistry, Russian Academy of Sciences; Kosygina str. 19, Moscow 119991, Russia.

[5] Friendly Solutions; Australia.

[6] WiscSIMS Lab, Dept. of Geoscience, Univ. of Wisconsin; Madison, WI, 53706, USA.

* Corresponding authors: adrien.vezinet@univ-grenoble-alpes.fr, aleksandr.chugunov@univ-grenoble-alpes.fr, alexander.sobolev@univ-grenoble-alpes.fr & stephan.sobolev@gfz-potsdam.de

† These authors contributed equally to this work

Abstract

The rates of continental crust growth and recycling on early Earth remain controversial because materials in the ancient crust and mantle have been altered, or even erased, by ongoing geodynamical processes. Melt inclusions in minerals are pockets of magma that have been trapped and shielded from the external environment. Where found within Archean high-Mg olivine – the first mineral to crystallize in mantle-derived melts – these inclusions can provide an unaltered glimpse of the geochemical state of the early Earth's mantle. We discovered an unprecedented unradiogenic Sr mantle source component ($^{87}Sr/^{86}Sr=0.69932\pm0.00024$, 95% c.i. here and below) in mantle-derived melts trapped in olivine from ca. 3.27 Ga komatiitic lava flows (Barberton Greenstone Belt, South Africa). This component shows a 4.31±0.19 Ga model age combined with significant chemical fractionation (Nb/U=36.9±1.5, Ce/Pb=16.7±1.1) translating to extraction, by the late-Hadean, of 80%±16% of mass of present-day continental crust assuming whole mantle processing. That agrees with the results of our geodynamic models explaining the Nb/U and Ce/Pb data by the production of 40 to 70% of the present-day continental crust mass during the Hadean in an oscillating mobile-lid tectonic regime with several tens of million years long periods of massive subduction induced by mantle plumes.

Main Text

Evolution of the early Earth and dynamics of its geochemical reservoirs are not well understood due to the near absence of Hadean (> 4.0 Ga) rocks and minerals preserved at the present-day Earth's surface[1,2]. Consequently, the rates of continental crust growth and recycling on the early Earth are still debated: estimates for the fraction of continental crust formed at the Hadean-Archean transition range between 0% and 100% of the volume of today's continental crust[3]. Several approaches have been used to provide estimates of continental crust volumes during the Hadean and Archean[3-7]. Studies assessing the degree of mantle depletion[4,6,7] are viewed as the most reliable since they account for both crustal extraction and recycling[3]. Most of these studies rely on the bulk rocks' Sm–Nd, Lu–Hf and U–Pb isotopic systems[3,4,6]. This approach, however, suffers from significant problems, such as known mantle heterogeneity on isotope ratios and systematic differences in these ratios of mid-ocean ridge basalts (MORB) and oceanic islands basalts (OIB) mantle sources[8]. In addition, the difference in isotopic effects of extraction and recycling of continental and oceanic crust or even fractionation effects at the magma ocean stage is not easily recognized[4]. Also, most ancient rocks are altered, which has been shown to affect Sm–Nd and Lu–Hf isotopic systems[9,10]. Further, whatever is the volume of continental crust on early Earth, the tectonic regime accounting for it remains debated, with suggestions being stagnant-lid, plutonic-squishy-lid, episodic-lid, mobile-lid, ridge-only and heat-pipe regimes[11,12].

Among the varied geochemical proxies that have been used over the past decades to decipher the production and recycling of continental crust, Nb/U and Ce/Pb in fresh lavas or glasses have received the most attention. These ratios are regarded as canonical because (i) they do not fractionate when the mantle rocks melt and (ii) are similar for present-day uncontaminated MORB and OIB[8,13,14] suggesting mantle homogeneity on these parameters. On the other hand,

Nb–U and Ce–Pb fractionate to give higher Nb/U and Ce/Pb values in the restite when hydrous mafic or ultramafic rocks melt in the crust or mantle, i.e., during the production of the felsic magmas (or their parentals) that form the bulk of continents[13]. This observation makes Nb/U and Ce/Pb ideal proxies to assess both the production of continental crust and recycling of restites through time[4].

Three aspects limit the accuracy of crustal growth curves built from Nb/U and Ce/Pb ratios measured in mantle-derived rocks. First, the timing of the generation of these ratios in the mantle source is unknown and could be much older than the eruption age of measured magmas. This means that mantle-evolution curves based on Nb/U or Ce/Pb ratios in mantle-derived melts[15] provide only lower estimates of the rate of crustal growth. Second, subduction of continental crust or/and unmelted oceanic crust to the source of mantle-derived magmas will decreases the Nb/U and Ce/Pb ratios of these melts, leading to underestimation of the extent of continental crust production. And third, the effect on these ratios of post-emplacement alteration, crustal assimilation and/or metamorphic overprinting is difficult to identify and quantify, leading to inaccurate interpretations[9,10,13].

Since olivine is the first mineral to crystallize in mantle-derived magmas, melt inclusions in high-Mg olivine crystals—those with high Mg# or Fo (=Mg/Mg+Fe molar%)—provide the most reliable information about parental melt compositions and the evolution of their mantle sources through time[15-20]. This stems from the capacity of melt inclusions to acquire the elemental and isotopic compositions of the host magma and preserve this information long after crystallization[16]. Consequently, melt inclusions in olivine (Figure 1) may provide a reliable view of the geochemical composition of the mantle source of melts.

The novelty of this study's results is twofold. First, we discovered a unradiogenic Sr mantle component previously unknown on Earth with unequivocal fractionated Nb/U and Ce/Pb values. These ratios are more uniform in the present-day mantle than Nd, Hf, and Pb isotopes[8,13,14] and explicitly mark the extraction of continental crust. Our Sr isotopes and Nb/U and Ce/Pb data came from pristine komatiite melt inclusions in olivine protected by the host mineral from alteration and suggest a significant event of continental crust extraction in Hadean time. Similar data on Nb/U and Ce/Pb of rocks are known only starting from 3.5 Ga and are compromised by their severe alteration. Second, we conducted advanced geodynamic modeling of the early Earth dynamics and extraction of the continental crust, coupled for the first time with the evolution of Rb-Sr isotope system and Nb, U, Ce, and Pb trace elements. This allows us to link geochemical data to the physical processes that might have been responsible for the observed evolution of chemical composition. In particular, using our models constrained by geochemical data we can discriminate between tectonic regimes that could have been active in Hadean and Eo-Archean time and suggest the preferred scenario of an oscillating mobile-lid tectonic regime with several tens of million years long periods of massive subduction induced by mantle plumes.

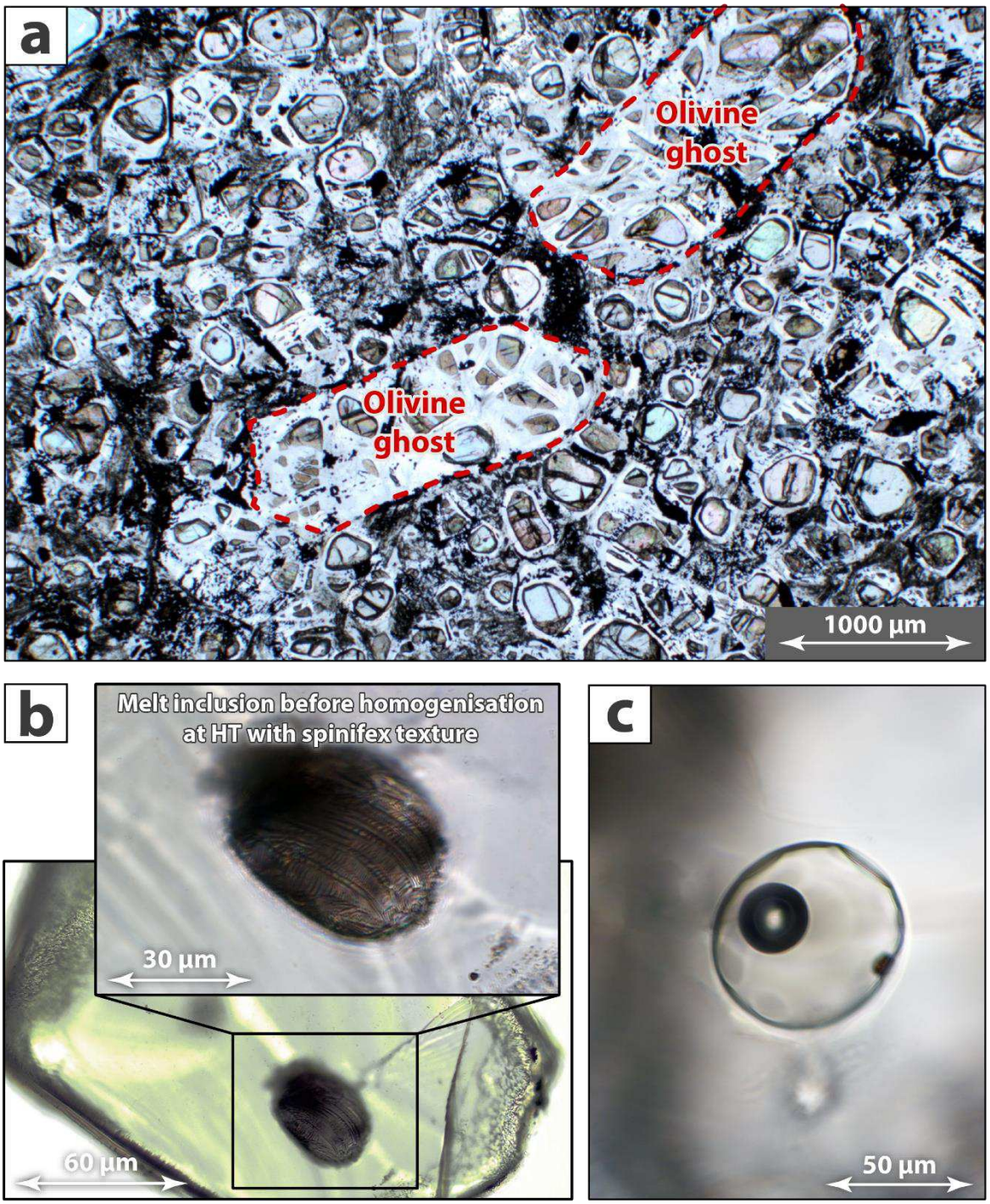

Figure 1: a. Olivine cumulate from Weltevreden Formation (sample 1528C) showing that although these cumulates are significantly altered, they still contain preserved unaltered olivine cores (plane polarized light). b. Partially crystallised natural (not annealed) olivine-hosted melt inclusion before homogenisation at high temperature. Inclusion consists of glass and acicular calcic pyroxene. c. Heated and quenched olivine-hosted melt inclusion consisting of glass, shrinkage bubble and spinel (dark crystal).

Weltevreden komatiites

We determined the chemical and isotopic compositions of olivine-hosted melt inclusions in samples from komatiitic flows from the *ca*. 3.27 Ga[ref. 21,22] Weltevreden Formation (Barberton Greenstone Belt, South Africa, Fig. S1). Whole-rock isotopic investigations indicate that the mantle sources of these komatiites experienced mantle depletion before eruption, possibly during the Hadean[23] (Figure S2). Here, using Sr-isotope signatures and trace-element contents measured directly in the homogeneous glass of melt inclusions (Figure 1c), we provide solid geochronological constraints for the timing of both the isolation of mantle domains from the Bulk Silicate Earth (BSE, also referred to as primitive mantle, PM) and the acquisition of canonical ratios indicative of continental crust extraction.

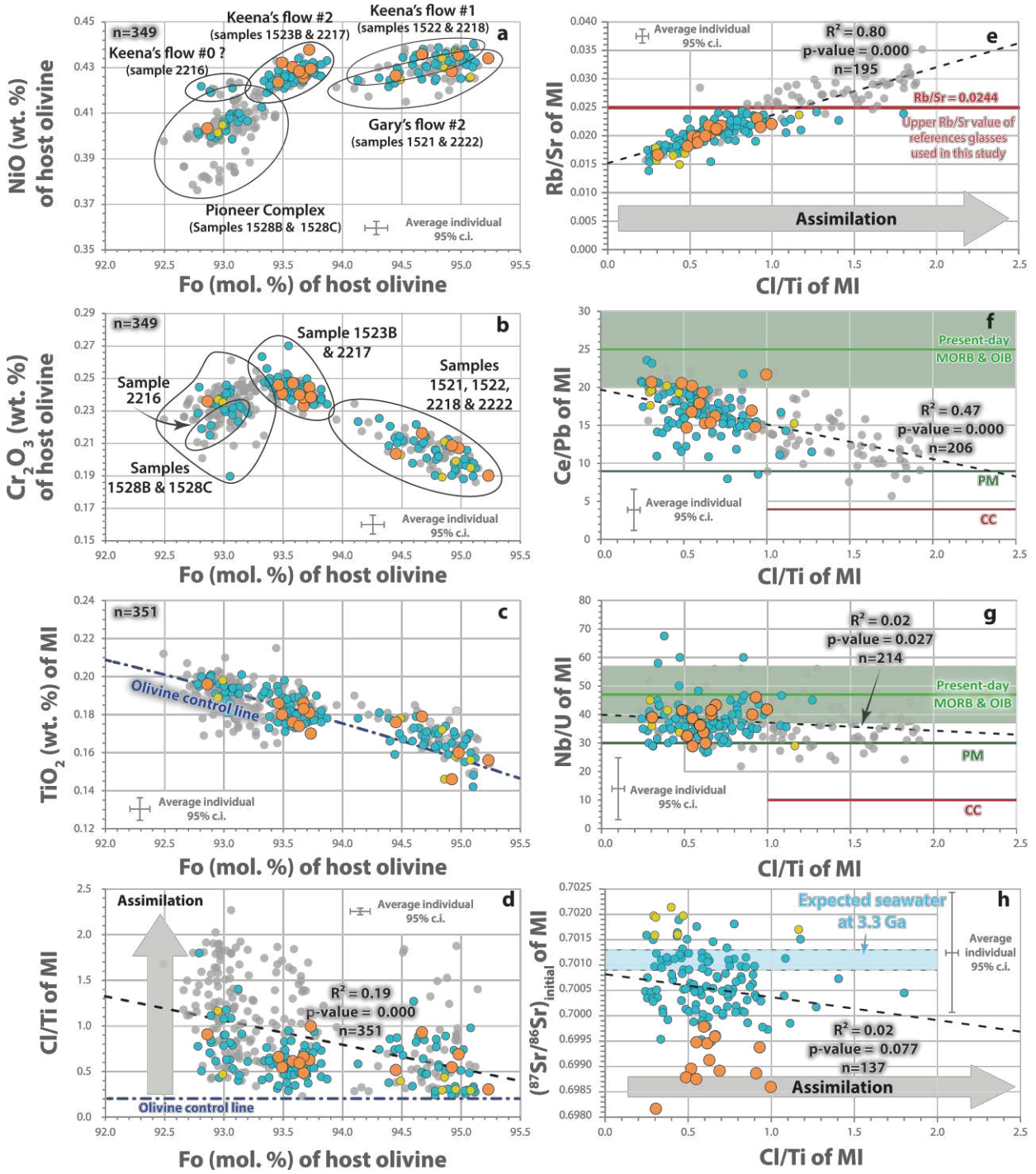

Figure 2: Contents of selected major, minor and trace elements and Sr isotopes in komatiite melt inclusions (MI) and host olivine crystals. Fo = 100Mg/(Mg+Fe) molar. Filled circles are those with a corresponding Sr-isotope analysis: blue for main group of melt inclusions, yellow for Sr-radiogenic melt inclusions, orange for Sr-unradiogenic melt inclusions (see below). Light grey circles are inclusions with no Sr data or rejected Sr isotope data because of Rb/Sr ratio over maximum value of used reference materials (0.0244) or uncertainty (2SE) of $^{87}Sr/^{86}Sr$ value > 0.0015 (SOM). Expected seawater[24]. Errors bars are average individual uncertainty at 95% confidence interval (c.i.). Outlines on figures 2a,b indicate samples from the same flows.

Melt inclusions in komatiite olivine phenocrysts

More than 350 olivine-hosted melt inclusions were selected and prepared for geochemical analyses. The analytical workflow, detailed in Methods, was as follows: (i) annealing of natural partly crystallized melt inclusions at high temperature and quenching to produce homogenous glass, (ii) electron microprobe analysis to determine major and minor elements in melt inclusions and host olivine, (iii) Raman-spectroscopy to determine H_2O contents of melt inclusions, and (iv) laser ablation split stream (LASS) ICP-MS analysis for Sr-isotope compositions and trace element contents of melt inclusions. Not all inclusions could be analyzed through the entire analytical workflow since LASS analysis requires a diameter ≥ 38 μm (optimal laser beam size) and only 195 inclusions satisfied this criterion. In addition, 19 more inclusions were analysed in single stream mode for trace elements.

Figure 2a and b present the composition of virtually unzoned olivine hosts of different isotopic groups of melt inclusions (see below) from five separate flows. The Fo and trace element contents (shown NiO and Cr_2O_3) of olivine differ both between and within flows. This variability suggests that the studied olivine crystals are, in fact, antecrysts that grew and trapped their melt inclusions in different places of a complex magmatic plumbing system. The TiO_2 contents of Weltevreden melt inclusions show a large variation, from ca. 0.14 wt. % to 0.21 wt. %, which is inversely correlated with host-olivine Fo contents (Figure 2c). This correlation follows a trend of *ca.* 33 wt% olivine extraction from the common parental melt (estimated from ingrowth of Ti from the melts trapped in the most Fo olivine) indicating that TiO_2 contents in the melt, as well as Al_2O_3 and CaO contents (not shown), are governed by olivine crystallization and extraction from parental melts with similar contents of these elements. Other proxies, such as Cl/Ti (Figure 2d-f), or K_2O/TiO_2 (Figure S3b-e), should remain constant in the melt during olivine

158 crystallization because of negligible contents of these elements in olivine. Clearly it is not the case. We attribute the large range of Cl/Ti and K_2O/TiO_2 for the same composition of host
160 olivine to assimilation into the komatiitic melts of small (*ca.* 1-2wt%) amounts of seawater-derived ultra-saline brine before emplacement at *ca*. 3.27 Ga (see Methods): a process common
162 for modern submarine basaltic melts[25,26] or larger amounts (e.g. 10%) of seawater-altered depleted serpentinite. Values of Cl/Ti can therefore be used as a proxy for such contamination. A
164 positive correlation is observed between Cl/Ti and Rb/Sr (Figure 2e) suggesting gain of Rb as well as Na, K, Pb, H_2O and Sr during contamination (Figure S3). To avoid samples significantly
166 affected by this process, we considered only melt inclusions with low Rb/Sr for geological interpretations in this study (Figure 2e). A maximum value of 0.0244 was selected for Rb/Sr
168 because it corresponds to the highest Rb/Sr value of the reference glasses used for LASS analysis (KL2-G, Figure S4). Unlike Rb/Sr, other proxies, such as Ce/Pb and Nb/U, show negative
170 correlation with Cl/Ti, suggesting that the higher values measured for these two ratios do not result from the contamination of the komatiitic melts before entrapment.

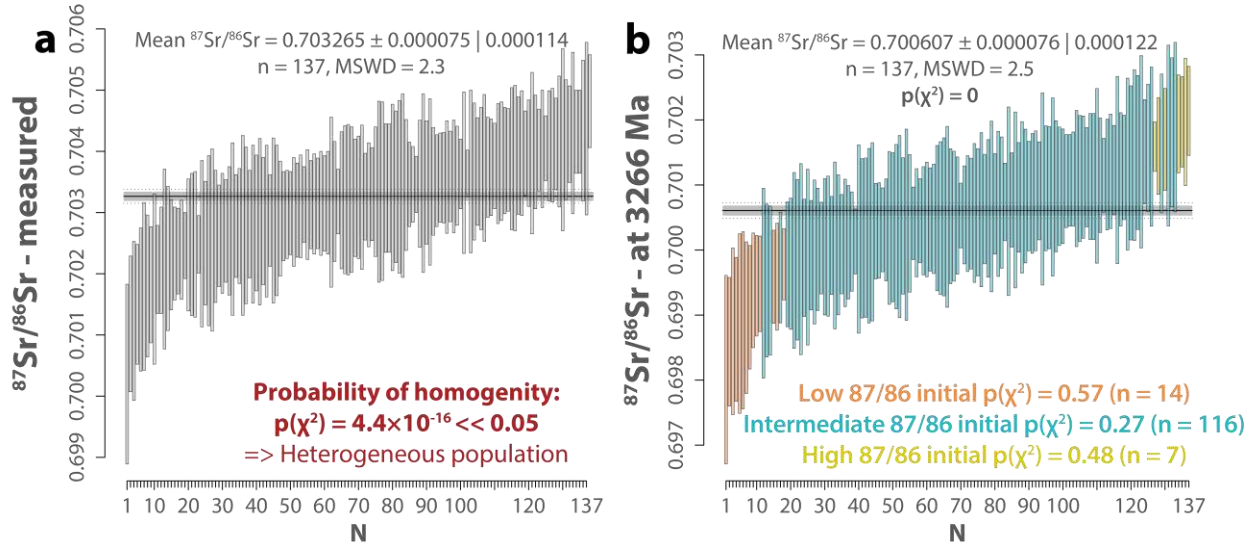

172 ***Figure 3: Sr-isotope of Weltevreden olivine-hosted melt inclusions. Both measured (panel a)***
174 ***and initial (panel b) $^{87}Sr/^{86}Sr$ values show low $p(\chi^2)$ (<< 0.05) indicating the lack of statistical homogeneity at the precision obtained for these Sr-isotope analyses. Three statistically***

homogenous groups can be distinguished in the data shown in panel b: unradiogenic in orange, radiogenic in yellow and neutral (main) in blue (see Methods for statistical treatment).

Sr isotopes and geochemical tracers in melt inclusions

The Sr-isotope signatures of Weltevreden melt inclusions show a large range of both measured and initial (back-calculated at 3266 Ma) $^{87}Sr/^{86}Sr$ values supported by $p(\chi^2)$ values << 0.05 indicating statistical heterogeneity within the whole dataset (***Figure 3***a,b). The effect of minor contamination of Weltevreden melts by seawater-derived brine or depleted serpentinite on their Sr isotope composition is within the analytical uncertainty, as seen by the lack of a significant correlation of $^{87}Sr/^{86}Sr$ value of melts and Cl/Ti, the chemical proxy of such contamination (see Figure 2h).

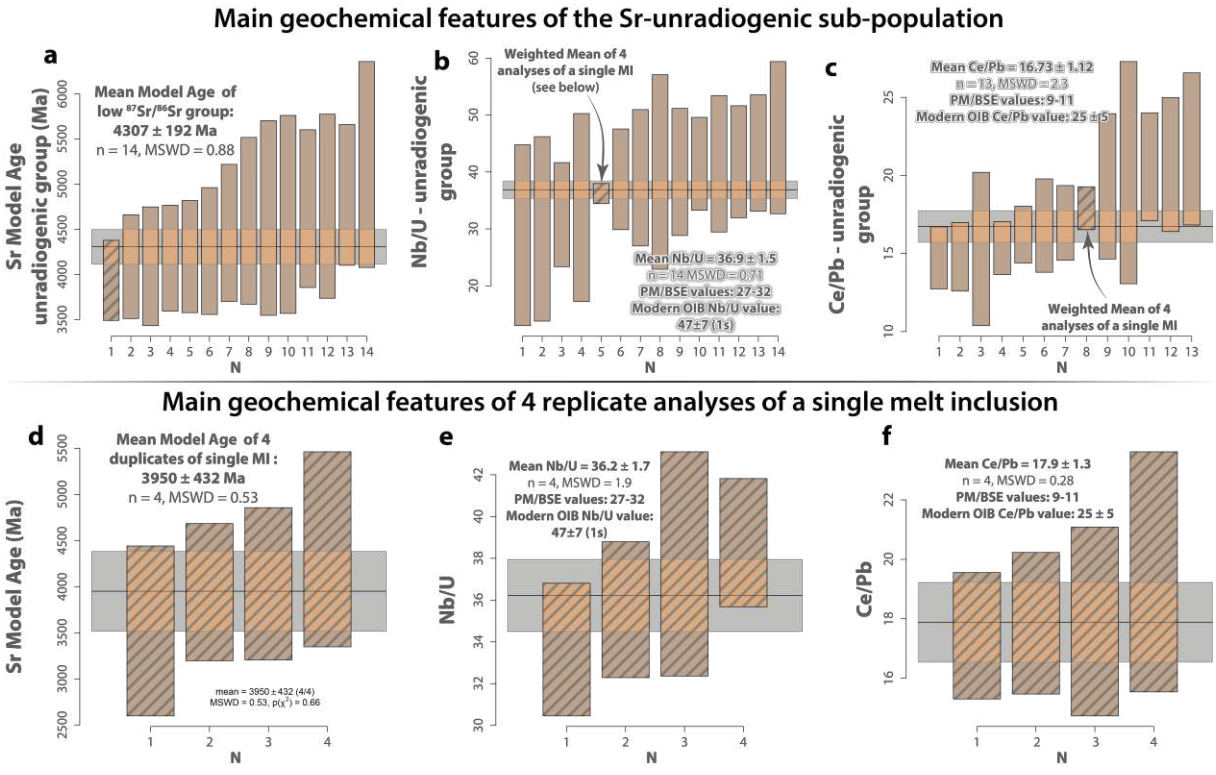

Figure 4. Sr-isotope and trace element signatures of the Weltevreden olivine-hosted melt inclusions of Sr-unradiogenic group. The Sr model age (see Methods) of the unradiogenic group (panel a) indicates mid-Hadean extraction from the Bulk Silicate Earth (BSE) while the Nb/U (panel b) and Ce/Pb (panel c) values of these-inclusions are significantly higher than those of primitive mantle (PM) or BSE, interpreted as reflecting restites after extraction of continental crust in the presence of H_2O during the Hadean. Panels d, e and f show results obtained on 4

replicate analyses of a single melt inclusion (MI) 2217-48-ol65 (belongs to of Sr-unradiogenic group) showing the robustness of our analytical protocol. Uncertainty bars are reported at a coverage factor of 2 (i.e., 95% confidence interval), (see Methods and Fig. S5 to S7).

A statistical analysis of our Sr-isotope dataset reveals three statistically homogenous groups based on their initial $^{87}Sr/^{86}Sr$ (see ***Figure 3***b and Methods for details). The means of initial $^{87}Sr/^{86}Sr$ values of these groups differ with confidence of over 99.9% (Supplementary Table 6). Out of these three groups, one, comprising 14 analyses, shows an extremely depleted $(^{87}Sr/^{86}Sr)_{initial}$ signature yielding a $(^{87}Sr/^{86}Sr)_{initial}$ weighted mean of 0.69932 ± 0.00024 (95% confidence interval, MSWD=0.88, $p(\chi^2)$=0.57, orange analyses in ***Figure 3***b). Olivine containing unradiogenic inclusions come from all studied flows (14 of total 137, thus 10%), but mostly (8 inclusions out of 14) from Keena's flow 2 (samples 1523B and 2217, Figure 2a,b, Fig. S1), where they compose 14% of 59 measured for Sr isotopes inclusions. The mean initial isotopic ratio of unradiogenic inclusions transposes to a Sr-model age, assuming no Rb in the source, of 4.31 ± 0.19 Ga (95% confidence interval, $p(\chi^2)$=0.57, Figure 4a) which we interpret to indicate that some components that melted to form Weltevreden komatiitic melts were geochemically isolated since the Hadean. Owing to the large radius of inclusion 2217-48-ol65, belonging to the unradiogenic group, four Sr-isotope & trace elements replicates were conducted. As demonstrated in Figure 4d,e,f and Supplementary Table 3d, all four replicate analyses form a statistically homogenous population for Sr isotopes and canonical ratios of interest, hence further validating the analytical approach developed in this study.

Continental crust extraction in the Hadean

Previous studies have used the geochemical proxy Nb/U to monitor the extent of continental crust extraction[4]. The weighted mean of the Nb/U values of the unradiogenic Sr melt inclusions is 36.9±1.5 (MSWD=0.71, n=14, Figure 4b). This value is significantly higher than all estimates

of the PM/BSE Nb/U values which lie between 26.7 and 32.4[ref. 8,27-29]. A similar observation can be made for the mean Ce/Pb value 16.73±1.12 (MSWD=2.3, n=13, Figure 4c) of this unradiogenic group, which is significantly higher than the PM/BSE value of 9-11.2 [ref. 8,27-29]. The four replicate obtained on inclusion 2217-48-ol65 show the same tendency (Figure 4d,e,f). The geochemical effect of Ca and Mg perovskite cumulation proposed for the source of Weltevreden komatiites[30] to explain moderate decoupling of Sm–Nd and Lu–Hf isotopic systems in their composition will produce Nb/U ratios in the source that are lower, not higher than in BSE/PM as observed in melt inclusions due to higher partition coefficient for U than for Nb in suggested mixture of Ca and Mg-perovskite[31]. In addition, similar and even much more significant decoupling of εNd and εHf is common in highly depleted abyssal and ophiolitic peridotites because of "following radiogenic ingrowth as a result of preferential fractionation of Lu/Hf during partial melting"[32]. The main mantle source component of studied komatiite was highly depleted mantle harzburgite as it follows from their contents of incompatible elements (including Sm-Nd and Lu-Hf), which are lower in parental melt than in BSE mantle[15]. Thus, the decoupling of εNd and εHf in their sources can be explained by the mantle restite of Eoarchean-Hadean age.

Extraction of continental crust from mafic crust and/or peridotite in the presence of H_2O followed by recycling of restite back to the mantle leads to depletion in Rb compared to Sr, Pb compared to Ce and U compared to Nb in the mixed deep mantle source. This explains the low Rb/Sr and high Ce/Pb and Nb/U values measured in mantle-derived melts[13]. However, the presence of subducted continental crust and unmelted mafic crust in the mantle source may significantly affect all these elemental ratios. Fortunately, the amount of such crust in the recovered Hadean component in Weltevreden melt inclusions is shown to be negligible by the exceptionally low contents of ^{87}Sr of the unradiogenic component. Thus, high Nb/U and Ce/Pb

ratios of unradiogenic-Sr melt inclusions are fully attributed to the production of continental crust. However, the estimated Sr isotope model age of the mixed source could reveal younger dates by few tens of million years, which are well within our reported ± 0.19 Ga uncertainty of the model age (see Fig. S7 and Methods).

The fraction of extracted continental crust produced from a specific domain of the mantle can be evaluated following the mass balance approach that has been adopted in previous studies[4] using our Nb/U values and Sr geochronological constraints together with the estimated Nb and U contents of the mantle[8,27-29] and continental crust[33-36]. First, the fraction of crust extracted from any volume of processed mantle can be estimated. Using the Nb/U weighted average of 36.9 ± 1.5 obtained on inclusions from source-rocks differentiated in the mid-Hadean, we estimate the fraction of extracted crust to be 0.43%±0.09% of the processed mantle. Assuming now 2.17×10^{22} kg as the mass of the present-day continental crust, 4.01×10^{24} kg as the mass of the whole mantle, the fraction of continental crust extracted in the Hadean, would be 80%±16% (Figure 5, orange dot) of the mass of the present-day continental crust. Similar calculation for individual melt inclusion 2217-48-ol65 yields 72%±24% (Figure 5, hatched orange dot). Such a high fraction, being the maximum value because it assumes the involvement of the whole mantle, still provides unprecedented evidence in support of earlier models arguing for massive continent production and recycling very early during Earth's history[3,6,37].

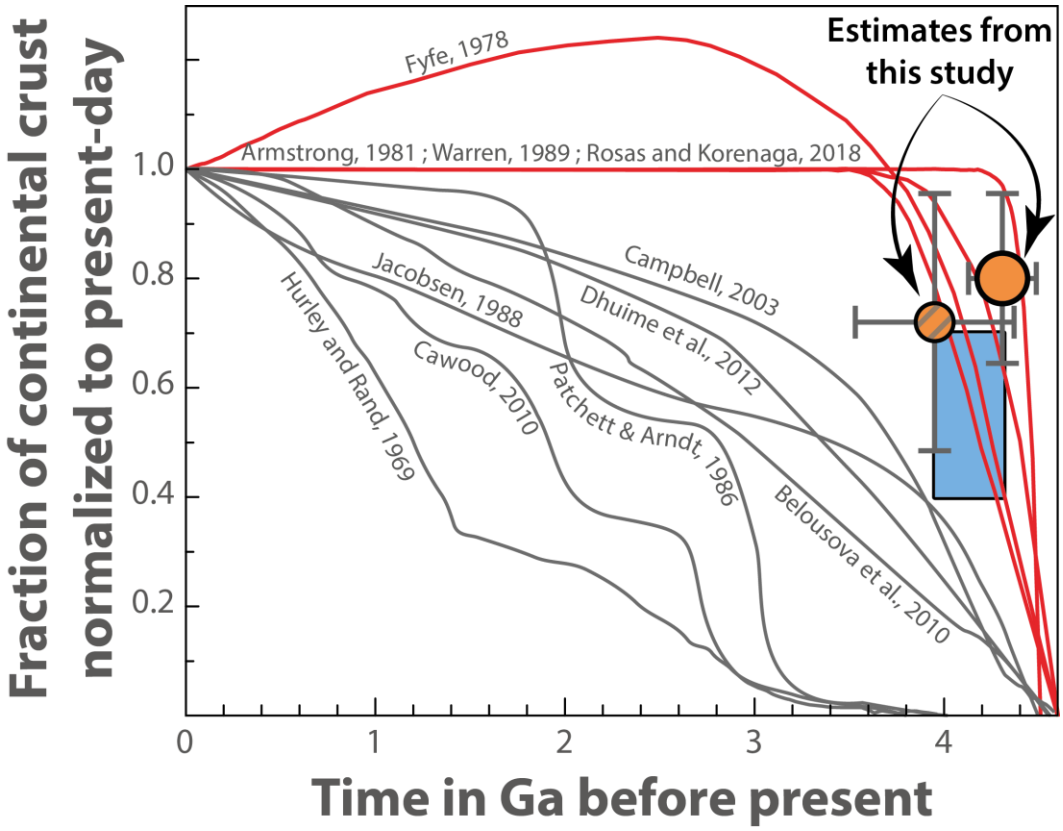

Figure 5: Compilation of previously published continental growth curves[3] and new estimate for the Hadean from this study (orange circles). These estimates have been obtained using measured average Nb/U value in the Sr-unradiogenic group large (orange dot) and individual inclusion 2217-48-ol65 (orange hatched dot) and the average of Nb and U values from four mantle models,[8,27-29] and four crustal models[33-36] assuming processing of whole mantle mass. Red curves are models in agreement with our results indicating continental crust production and subsequent recycling of restites in the Hadean. Uncertainty bars are reported at a coverage factor of 2 (i.e., 95% confidence interval). Light blue field shows the range of continental crust fractions produced during Hadean which according to the geodynamic models fit best geochemical data (see below Geodynamic modelling section).

Our new results interpreted as indicating that a large fraction of continental crust was extracted, and its residue was recycled into the mantle very early in Earth history is consistent with the composition of ancient zircons[38,39], the radiogenic isotope compositions of bulk rocks[40] and numerical modelling (see Geodynamic modelling). Elevated Nb/U and Ce/Pb values obtained in deeply-sourced Weltevreden komatiitic melts indicates efficient, vertical, transfer (subduction of oceanic crust residue after partial melting producing felsic crust) between the upper and the

lower mantle in the Hadean. Although the geochemical results presented here indicate significant continental crust production in early Earth time, the tectonic regime accounting for the formation of this crust and actual mass of mantle processed cannot be extracted from such a geochemical dataset. To complete the picture, geodynamic modelling, within which $^{87}Sr/^{86}Sr$, Nb/U and Ce/Pb geochemical proxies were monitored in order to identify the configuration/regime best-reproducing the measured geochemical information.

Geodynamic modelling

We used the mantle convection code StagYY[41], which has been extensively used over the last decades for the modelling of coupled core-mantle-crust evolution of rocky planets. With a 2D spherical annulus domain[42], our models generate both basaltic and felsic melts[43], include cooling of the core, and use pressure- and temperature- dependent water solubility maps for different mantle minerals[11]. For this study, we improved previous models[11,43] by including the effect of water on the density of mantle materials, by incorporating a composite rheology (diffusion creep and dislocation creep proxy) for the upper mantle based on experimental data, and by initializing the frictional strength of the early Earth's oceanic lithosphere based on experimental data. Following approaches from previous studies[44,45], we included the evolution of Rb-Sr isotopes as well as Nb, U, Ce and Pb trace elements in these geodynamic models (see Methods for further details). We computed a series of models by varying lithosphere's hydration and frictional strength (see Methods for model setup).

Our numerical experiments start with a homogeneous solid Earth of pyrolytic (BSE) composition[27] at 4.5 Ga with a low (0.01 wt. %) initial water content[11], mantle potential temperature of 1900 K and a core temperature of 5000 K. They end after 1.5 billion years, i.e. at

3.0 Ga. Any cataclysm relating to the formation of the mantle or the Moon is assumed to be earlier than 4.5 Ga.

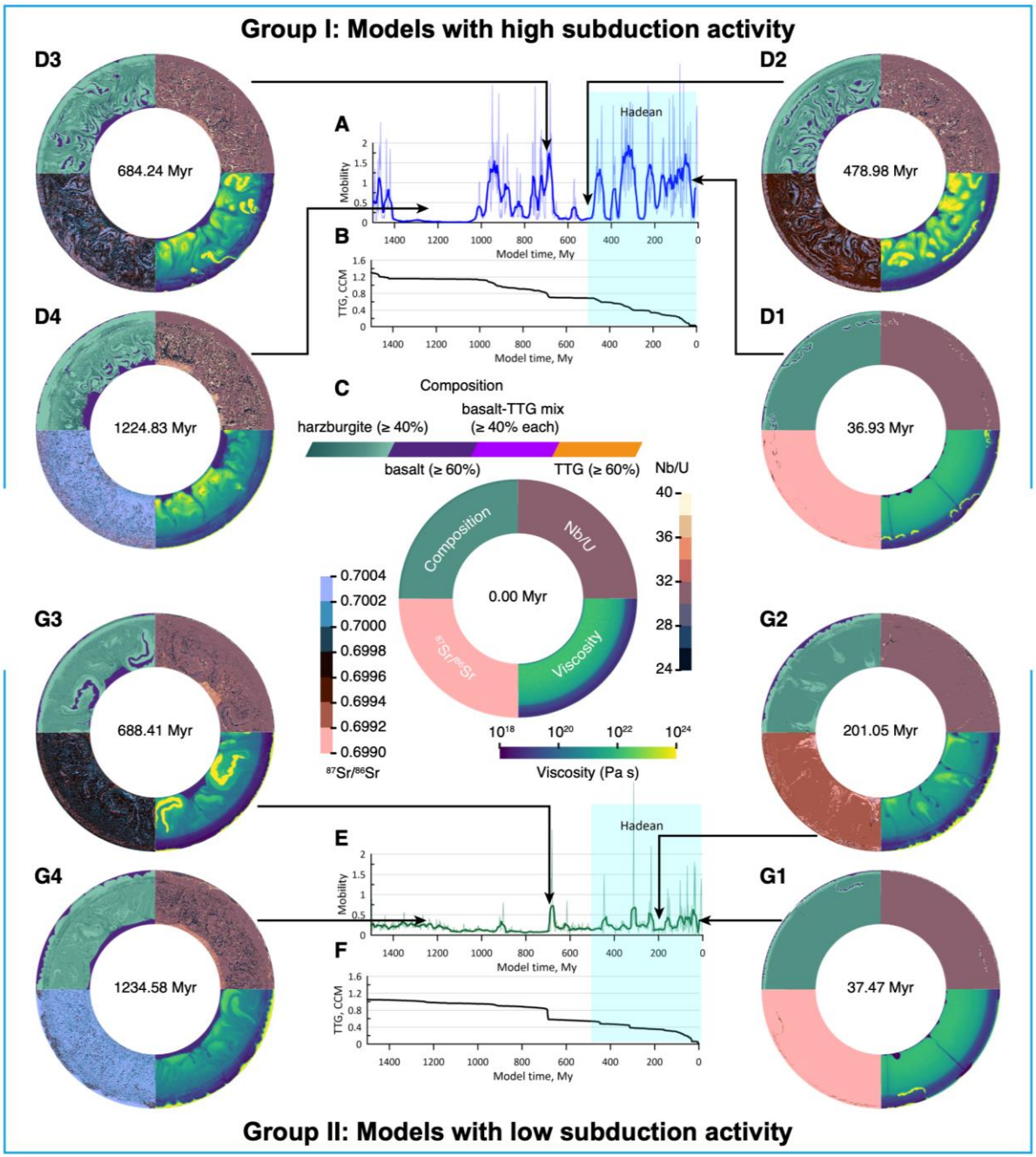

Figure 6: Representative models from Group I (A,B,D1-D4) and Group II (E,F,G1-G4). (A,E) Mobility of models over time with a moving average (thick line) over 11 mobility values (thin lines). (B,F) Mass of generated continental crust over time, scaled with the present-day

continental crust mass(CCM). (C,D1-D4,G1-G4) Snapshots of Earth's cross sectionshowing the evolution of models with time where four quadrants represent different fields (clockwise from top left: composition, Nb/U, viscosity, $^{87}Sr/^{86}Sr$). Snapshot (C) shows initial model state corresponding to an age of 4500 Ma and model time of 0 Myr. Snapshots (D1,G1) show periods of active subduction, while snapshots (D2,D4,G2,G4) show periods of lulls in subduction activity where large mantle plumes (dark blue in the viscosity field) are trapped beneath the cold recycled material (yellow in the viscosity field). (E) shows a mobility burst at ca. 680 Myr of model time characterised by a resurfacing event (G3) and a spike in the production of continental crust (F).

All models fall into two different groups. The Group I consists of models with our preferred effective friction coefficient of the lithosphere for the early Earth of 0.1[ref.46], while Group II consists of the models with higher lithospheric strength. The representative models from both groups are shown in Figure 6. Typical behavior of all models is intense mantle convection during the first hundred million years (Figure 6D1, G1), when multiple large hot mantle plumes form at the core-mantle boundary (CMB) and repeatedly approach the lithosphere. Plumes break the lithosphere and induce its subduction (Figure 6D1, G1). During this stage, there is extensive production of both oceanic and continental crust (Figure 6B, F). The following evolution depends on the lithospheric strength and is best described by the so-called mobility function which represents a ratio of the root-mean-square (rms) of the surface velocity averaged over the rms velocity of the entire computational domain [47]. Mobility value above 1 means that lithosphere moves horizontally relative to underlying mantle with significant velocities and subduction is active[12].

In models of Group I, high mobility periods last several tens of million years and interchange with the low mobility periods (Figure 6A). We call this tectonic regime an oscillating mobile-lid regime. High mobility periods correspond to periods of extensive crustal production and lithospheric subduction and result in an accumulation of a large amount of cold recycled material at the CMB, which hinders the propagation of large mantle plumes (Figure 6D2). The plumes

that manage to rise through this overlying cold recycled material are small and are not able to break the lithosphere or induce subduction, resulting in a reduced production of new crust (and more recycling of existing crust) of the crust (Figure 6B, model time range 450-700 Myr). Then it takes a few hundred million years to heat this cold material that sits above the CMB. Thus, there is a period of quiescence before large plumes break through, approach the lithosphere and induce new subduction zones, which produce and recycle new crust (Figure 6B, D3).

Group II models are characterized by low mobility throughout the evolution and experience several mobility bursts that last several million years (Figure 6E). This type of tectonic regime is usually called episodic-lid regime[12]. During these episodes of high mobility, the overthickened lithosphere is rapidly subducted resulting in resurfacing events (Figure 6G3). Most of the continental crust is produced during these events. Note that despite showcasing different tectonic regimes, the models from both groups may produce similar amounts of continental crust and most of it during Hadean (Figure 6B,F), while models of Group II require for a larger input of the surface water.

In all models, at every time step we identify regions of hot material (potential temperature above 1700°C) in the transition zone as the potential sources of komatiites (see Methods for details) and select the model's cells that represent Hadean fraction of material with the $^{87}Sr/^{86}Sr$ ratio < 0.6997. The evolution of the trace element ratios in the Hadean fraction for a number of models from both groups are presented in Figure 7a,e and Figure 8a,e. The common feature of all models is that trace elements do not show any effect of continental crust production till at least 500 Myr of model time (i.e., 4.0 Ga) even though the continental crust production during the first 500 Myr is more than twice that of the last 1000 Myr in most models. This time lag indicates the

time required by the hydrated basaltic crust, which was involved in the production of continental crust to recycle and mix with the plume source material in the lower mantle.

The models of Group I that produce 40 to 70% of present-day continental crust mass (CCM) during the Hadean, show a good fit with the Nb/U and Ce/Pb data at the time close to the emplacement of Weltevreden komatiites at 3267 Ma (i.e., model time of 1230 Myr, Figure 5 and Figure 7a,d). These models also predict a realistic amount of Hadean component in plumes (Figure 7c,f) and a rather moderate supply of water into the lithosphere (0.5-0.9 present-day ocean mass (OM)) over the period of 1500 Myr. In contrast, the models of Group II where we chose the water input parameters such that the models produce the similar amount of continental crust during the Hadean as the models of Group I, show a poor fit with Nb/U and Ce/Pb data (Figure 8a.d), a too low amount of Hadean component in plumes (Figure 8c,d) and predict a water supply of 1.1-2.5 OM into the lithosphere over the period of 1500 Myr. The reason behind these different model predictions is the much lower recycling rate of the lithosphere in the models of Group II where the mobility, and therefore the subduction activity, are lower than in Group I models.

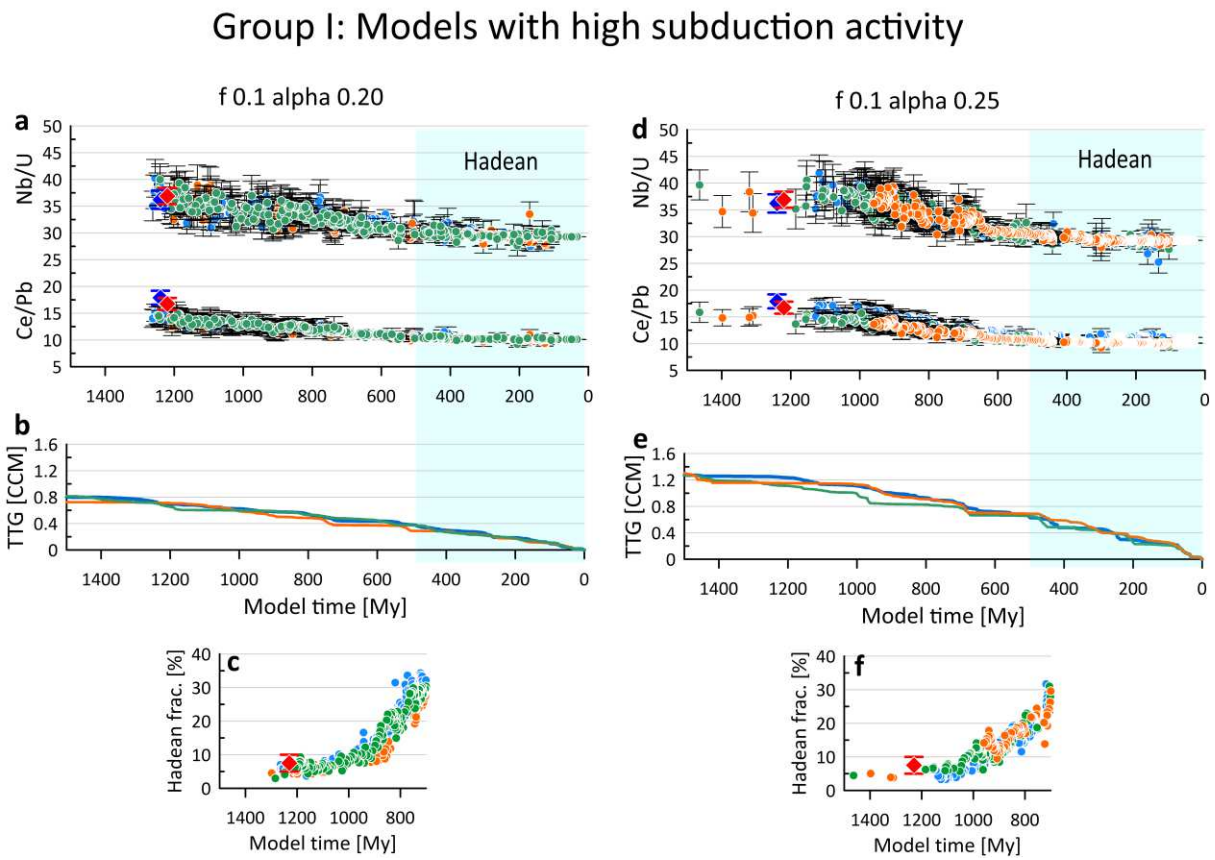

Figure 7: A subset of resuls of models of Group I compared with observations. (a,d)- Evolution of trace element ratios Nb/U and Ce/Pb in the Hadean fraction (with $^{87}Sr/^{86}Sr < 0.6997$) of hot plume material in the transition zone from multiple models with different lithospheric hydration (see Methods for details). Each colored solid circle represents mean trace element ratio for the selected cells with error bars with 2 standard deviations of mean value. (b,e)- Mass of generated continental crust over time from the same models, scaled with the present-day continental crust mass. (c,f)-Amount of Hadean fraction in the hot plume material from the same models. Red solid diamonds (main Hadean group data) and blue diamonds (single inclusion data) show geochemical observations with error bars of 2 standard deviations of mean value.

Our models infer that in order to fit the geochemical observations, the following two conditions must have been fulfilled. First, the water supply into the lithosphere must have been high enough to allow for ca 40 to 70% of CCM production of continental crust during the Hadean in agreement with maximal estimates of 50 to 100% of CCM using mass balance apprpoach

assuming whole mantle processing (Figure 5). Second, the tectonic regime in the Hadean and the Eo-Archean time must have been sufficiently mobile, i.e. with periods of extensive subduction. Classical episodic regimes with rare partial resurfacing and sagduction or stagnant lid regime are not consistent with geochemical observations. We note that “subduction” in our models, defined as sinking into the mantle of the pieces of the entire upper thermal boundary layer (lid) including its surface, does not look like the present-day continuous and stable subduction that is characteristic of Phanerozoic plate tectonics. It is much more variable and short-lived. Moreover, our models show that in Hadean-Archean Earth in contrast to the present-day Earth, large mantle plumes are of key importance to trigger such subduction and when plume activity is diminished, the subduction activity is also diminished.

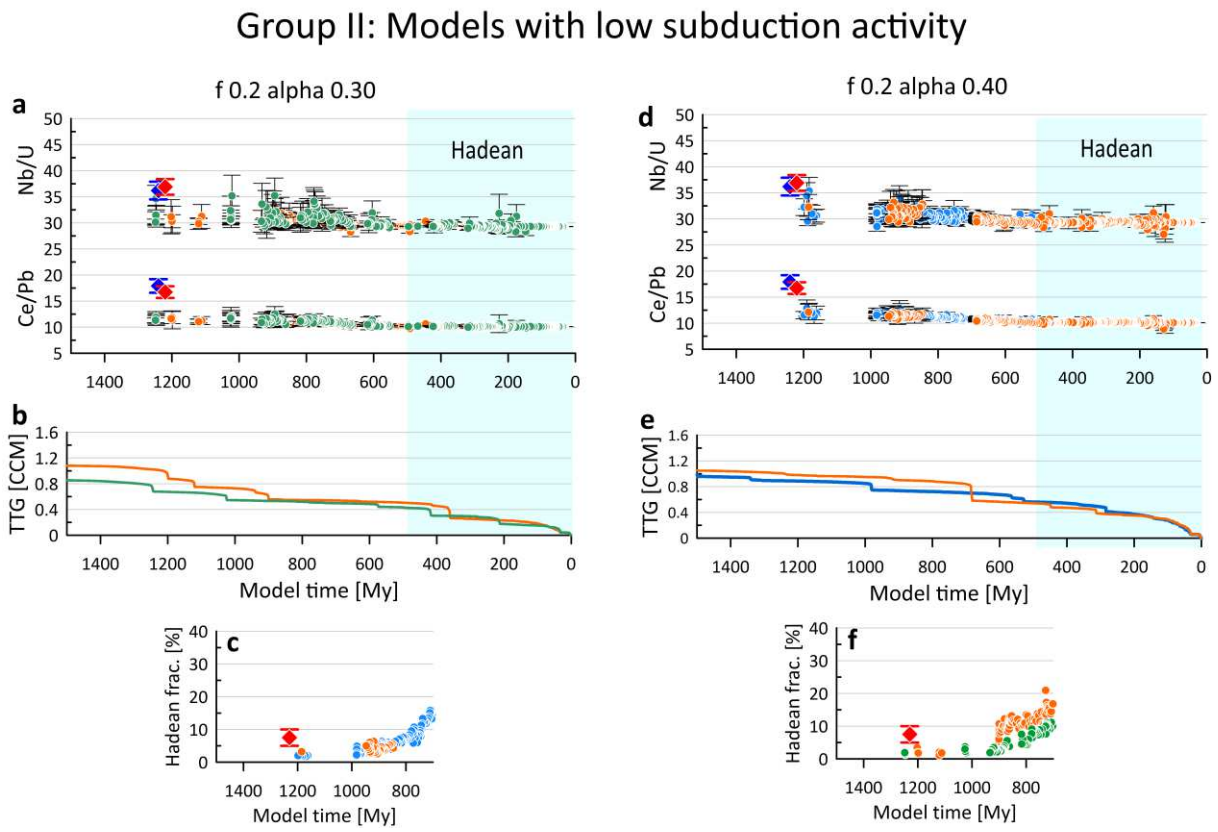

406 ***Figure 8: A subset of results of models of Group II compared with observations. The legend is the same as in Figure 7. Note poor fit of the geochemical data (red and blue diamonds)***
408 ***compared with the models of Group I shown in Figure 7.***

410 Altogether, the geochemical data and geodynamic models presented in this study indicate that large volumes of both oceanic and continental crust had already formed and recycled by the late-
412 Hadean, thereby favoring the—still contentious—model presented by Richard Armstrong more than four decades ago[37] as well as several recent models[3,6]

414

416

Methods

Methods for geochemical investigation

- **Samples**

The eight olivine-cumulates were sampled in the best-preserved parts of individual komatiite flows in the Saw Mill and Pioneer Complexes of the Weltevreden Formation of the Barberton greenstone Belt, South Africa, Fig. S 1). These cumulates consist of partially altered olivine crystals, and ground mass spinel and clinopyroxene grains enclosed in a matrix of altered glass (chlorite and amphibole). Three samples (1521, 1522 and 1523) from the Saw Mill Complex were previously described[15]. Sample 2216 (Gary's flow 1, 25.842597°S, 30.885031°E) is an olivine cumulate that contains large (up to 2 mm in diameter) partially serpentinized euhedral olivine grains with high Fo contents (92.8–93.1 mol.% Fo). The interstitial groundmass of the rock is made of acicular clinopyroxene (0.5-1 mm long), equant or skeletal spinel (up to 50 μm in diameter), and altered volcanic glass. Sample 2217 (Keena's flow 2, 25.841475°S, 30.885683°E) is an olivine cumulate consisting of best preserved out of all samples, but still partially serpentinized, euhedral olivine grains of different size (mainly 0.6–1 mm, with individual grains up to 1.5 mm in diameter; 93.2–93.8 mol.% Fo). The interstitial groundmass is made of acicular clinopyroxene (up to 1 mm long), equant and skeletal spinel crystals (up to 100 μm in diameter) and altered volcanic glass. Sample 2218 (Keena's flow 1, 25.841803°S, 30.886147°E) is an olivine cumulate consisting of partially serpentinized euhedral olivine grains of different size (mainly 0.5–2 mm, with exceptional grains up to 4 mm in length; 94.6–95.1 mol.% Fo). The interstitial groundmass is made of acicular clinopyroxene (up to 0.5 mm long), equant and skeletal spinel crystals (up to 100 μm in diameter) and altered volcanic glass. Sample 2222 (Gary's flow 2, 25.843578°S, 30.887742°E) is an olivine cumulate that contains large (up

to 2 mm in diameter) partially serpentinized euhedral olivine grains with high Fo contents (94.8–
442 95.2 mol.% Fo). The interstitial groundmass of the rock is made of clinopyroxene (up to 1 mm long), equant spinel (up to 100 μm in diameter) and altered volcanic glass. Sample 1528 from the
444 Pioneer Complex (25.834308°S, 30.949083°E) is an olivine cumulate consisting of partially serpentinized euhedral olivine grains or olivine pseudomorphs of different size (mainly 0.5–1.5
446 mm; 92.5–93.5 mol.% Fo, Figure 1, main text). The interstitial groundmass is made of acicular clinopyroxene (up to 1 mm long), equant and skeletal spinel crystals (up to 100 μm in diameter)
448 and altered volcanic glass.

- **Melt inclusions**

450 Prior to polishing and mounting, melt inclusions hosted in olivine crystals were homogenized at high temperature and 1 atm. To homogenize partially crystallized melt inclusions, olivine
452 crystals were placed in open platinum ampoules and heated in a vertical high-temperature furnace at Vernadsky Institute of Geochemistry (Moscow) following previously established
454 protocol[17]. Target temperatures for experiments range from 1280°C to 1350°C in order to complete melting of crystalline phases in inclusions, and to minimize diffusional loss of
456 hydrogen from inclusions through the host olivine. Upon heating completion, instantaneous quenching of the melt inclusion is achieved via immersing ampoules in water at room
458 temperature. Because inclusions were heated at 1 atm pressure under reduced gas flow, all inclusions which were opened even partly lost their volatiles: e.g. Cl, S, H_2O as well as part of
460 Na and most of Pb. Such inclusions, which can be identified by electron microprobe analysis, have Cl and S typically below detection limit, and were neglected in this study. Correction of the
462 measured composition of glass in melt inclusions (see below) for post entrapment olivine crystallisation on the walls of inclusion's cavity and Fe-Mg exchange with host olivine (PEC)
464 was performed using Petrolog 3 software software[48]. Details on this approach are reported in

earlier studies[15]. PEC corrected inclusions compositions presented in SupplementaryTables 4 and 5.

- **Electron microprobe analyses**

The chemical composition of the olivine and melt inclusions were analysed using a JEOL JXA-8230 electron microprobe and a JEOL FEG JXA-iHP200F electron microprobe at ISTerre Micro-Analytical Platform (IMAP), Université Grenoble Alpes (France) using an analytical protocol published eslwhere[49]. The Mg-Fe olivine-melt geothermometer was used for the estimation of komatiitic melt inclusion crystallization/entrapment temperature, with correction for the effects of measured water contents[50].

- **Raman microscope**

Water content of melt inclusions was determined using Raman microscope LABRAM Soleil, Horiba (ISTerre, Grenoble, France), equipped with 473 nm and 532 nm lasers and optical microscope (Nikon Eclipse LVDIA-N) using an analytical protocol previously published[49]. Average and 2SE uncertainties are reported in the SupplementaryTables 3, 4 and 5.

- **Laser Ablation Split Stream (LASS) ICP–MS analyses**

LA–ICP–MS analyses were conducted at IMAP (Université Grenoble Alpes, France). Strontium (Sr) isotope signatures and trace element (TE) contents were measured directly in melt inclusions with a laser ablation (LA) system (RESOlution SE, Applied Spectra) coupled with multi-collector (Neptune XT, Thermo Fisher Scientific) for Sr-isotope and single-collector (8900, Agilent) for TE inductively-coupled plasma mass spectrometer (ICP-MS). LA single stream and LA split stream (LASS) protocols were used depending on the size of the melt inclusions: smaller inclusions were analyzed with our LASS Sr-TE analytical protocol while bigger ones had two laser analyses, one for Sr-isotopes and one for TE's. Uncertainties are reported at 95%

488 confidence interval unless stated otherwise. It is worth mentioning that Sr content in Weltevreden melt inclusions average 36±6 ppm, corresponding to a mass of total Sr of ca. 6 pg
490 in most melt inclusions. Currently, such small amounts of Sr cannot be accurately measured via the traditionally more precise TIMS approach owing to the lowest Sr blanks obtained through
492 such approach a few tenths of pg[51].

Sr-isotope compositions were measured on a Neptune XT MC–ICP–MS (Thermo-Fisher
494 Scientific) following conventional cup configurations. Additionally, we also measured mass 90 in order to evaluate the Sr/Zr of Weltevreden melt inclusions and compare these ratios with the
496 trace element data obtained concurrently. Measurements were conducted in static mode and all signals were collected in Faraday cups. Four 10^{13} Ω amplifiers were used for the measurement of
498 masses 84, 85, 86 and 87. All other masses (83, 83.5, 86.5, 88 and 90) were measured with 10^{11} Ω amplifiers. Gain calibration was conducted overnight before each analytical run of melt
500 inclusions. Integration time was set to 1.049 seconds. The instrument was run in low-resolution mode (mass resolution of ca. 400). Ni Jet-Sampler and Ni X-Skimmer cones were used. Sr-
502 isotope analyses were reduced offline using an in-house modified python code compatible with Iolite-4[52]. All channels were first background subtracted. Since 83.5 and 86.5 signals were
504 always below detection limit (calculated as 3.29 × standard deviation of the background over the entire analytical run[53]), no REE^{2+} correction was conducted. Calcium-argides (Ca–Ar) species,
506 which can cause interference on masses 84, 86 and 88) are corrected using the background subtracted signal of mass 83. A power-law based Sr-fractionation factor (β^{Sr}) was then calculated
508 for each individual analysis based on the measured (88/86) value and the natural value (8.37520938). The Rb fractionation factor (β^{Rb}) was manually adjusted to provide the best
510 accuracy for all three reference materials measured throughout the analytical run. This approach allows to account for day-to-day variations in β^{Rb} and is analogous to the approach used for

correcting Yb interference in zircon Hf-isotope analysis. The amount of ^{87}Rb is then calculated using the measured ^{85}Rb and the natural $^{87}Rb/^{85}Rb$ value (0.38571). Then, the amount of ^{87}Sr is obtained via removing the contribution of ^{87}Rb on the measured 87 signals (87 net signal = ^{87}Rb + ^{87}Sr). Isotopic ratios are then calculated including a power-law based mass bias correction. For all melt inclusions labelled 15XX, adjusting β^{Rb} value on daily basis was sufficient to obtain accurate results (within 2SD) for all three reference glasses covering all compositional range of measured inclusions used in each analytical run (KL2-G, NIST-614-G and GOR128-G, see Fig. S 4), no standardization of the data was conducted here for $^{87}Sr/^{86}Sr$ values. Standardization was however required for $^{87}Rb/^{86}Sr$, and Sr/Zr values. This is likely the result of minor elemental fractionation causing inaccuracy for corrected-only ratios. For melt inclusions labelled 22XX, standardization of both $^{87}Sr/^{86}Sr$ and $^{87}Rb/^{86}Sr$ was conducted with KL2-G as calibration glass. Readers can refer to the Sr-isotope DRS provided on the Iolite Github (https://github.com/iolite-LA-ICP-MS) for full view of the python code. Individual analysis uncertainties are calculated by the in-house built Iolite code. Hence, exports from Iolite include uncertainties of all background, interference corrections and standardization if conducted. Note that including REE^{2+} correction changes the final uncertainty to the sixth decimal only, i.e., 2 orders of magnitude lower than typical precision obtained with our LASS protocol for such Sr-depleted melt inclusions. Since several analytical runs were conducted for analyzing these melt inclusions, an evaluation of the inter-sequence (i.e. long-term) excess variance (i.e. long-term variance) was conducted. This approach follows the widely accepted workflow used in U–Pb isotope analyses[54] and consists of calculating the degree of homogeneity of the reference glasses over all sequence: if the MSWD value—or corresponding $p(\chi^2)$ value—is within acceptable range of 5–95%, then no inter-sequence excess variance is propagated into individual analyses. If not, then uncertainties are expanded up to the level where all validation materials (here glasses) return MSDW value or

536 p(χ^2) value indicating statistical homogeneity. No inter-sequence excess variance was required for the $^{87}Sr/^{86}Sr$ values: MSWD and p(χ^2) values for the three reference glasses GOR128-G,
538 KL2-G and NIST-614-G are: (i) 1.16 and 8.9%, (ii) 0.41 and 100%, (iii) 1.02 and 43% respectively (see data in Supplementary Table 1), while an inter-sequence excess variance of
540 5.5%, 6% and 6% was propagated into $^{87}Rb/^{86}Sr$ and Sr/Zr values respectively for all analyses (reference glasses and melt inclusions). Similar to the standardization mentioned above, the need
542 of inter-sequence excess variance for these ratios likely reflects the contribution of elemental fractionation, which is unaccounted for in our data reduction protocol; an effect absents from
544 $^{87}Sr/^{86}Sr$ calculation, hence explaining the better accuracy over several analytical runs for this latter ratio. Consequently, we consider the uncertainty reported in individual $^{87}Sr/^{86}Sr$, $^{87}Rb/^{86}Sr$
546 and Sr/Zr values as external uncertainty. Precision and accuracy of Sr isotope analyses of melt inclusions were double checked by duplicate, triplicate or quatroplicate analyses of sufficiently
548 large inclusions (Supplementary Fig. S 5 and Table 3c). The homogeneity of the replicates of 2, 3 or 4 analyses of the same melt inclusion presented in this diagram confirms that reported
550 uncertainties of individual inclusions are not underestimated.

All melt inclusions discussed in this work have $^{87}Rb/^{86}Sr$ values lower than the $^{87}Rb/^{86}Sr$ of KL2-
552 G (0.069898), the reference glass with the most elevated $^{87}Rb/^{86}Sr$. Melt inclusions displaying $^{87}Rb/^{86}Sr$ higher than KL2-G were disregarded since the accuracy of the ^{87}Rb correction could
554 not be assessed. In addition, inclusions with 2 standard errors of measured $^{87}Sr/^{86}Sr$ ratio over ± 0.0015 (thin inclusions where signal was collected for less than 8 seconds), were also excluded.
556 Lastly, we checked robustness of $^{87}Sr/^{86}Sr$ errors of accepted individual inclusions by comparison with the errors of reference materials using the following equation:

558 $$\sigma_{inclusion} = \sigma_{RM} \times \sqrt{\frac{Sr_{RM} \times t_{RM}}{Sr_{inclusion} \times t_{inclusion}}}$$

Where $\sigma_{inclusion}$ and σ_{RM} are 95% c.i. uncertainties of individual inclusions and reference material (glasses) respectively; $Sr_{inclusion}$ and Sr_{RM} are Sr contents in inclusions and reference materials; $t_{inclusion}$and t_{RM} *are* $^{87}Sr/^{86}Sr$ acquisition times for inclusions and reference materials (Supplementary Table 2).

Both predicted average $\sigma_{inclusion}$ calculated for all Weltevreden melt inclusions and for the 14 unradiogenic ones as well as their measured $\sigma_{inclusion}$ are 0.0010, thus virtually identical (Supplementary Table 2). We therefore conclude that reported errors of $^{87}Sr/^{86}Sr$ ratios for individual melt inclusions are neither over nor underestimated and thus are valid for statistical treatment.

TE analyses were conducted with 20-µm spots/10-Hz pulse frequency and 38-µm spots/15-Hz pulse frequency for inclusions in single and split stream mode respectively and a laser fluence of 4 J.cm^{-2}. Carrier gas was He (*ca.* 0.3-0.9 L/min) with addition of N_2 (*ca.*1 to 2.5 mL/min) which were mixed with Ar (*ca*. 0.6-1.1 L/min) before introduction into spectrometer. Oxide production rate, monitored with ThO^+/Th^+ was < 0.1%, and the doubly charged ratio monitored with $^{44}Ca^{2+}/^{44}Ca^+$ was < 0.1%. The U/Th ratio ranged between 98% and 102%. Analyses were conducted in time-resolved acquisition mode (TRA) and included 1 second of pre-ablation to eliminate surface contamination, 30-40 s background measurement followed by 30-40 s sample ablation and signal measurement. Dwell time was 10-100 ms for different elements. All spectra were inspected in LADR software to define intervals for integration and exclude remaining surface contamination, if any. Concentrations were quantified from the measured ion yields normalized to Ca, previously measured on EPMA. Details on the varied sweep times and TE data reduction are reported in SupplementaryTable 3a. Ce/Pb, Nb/U and Rb/Sr of reference glasses (GOR128-G[55] and NIST614-G[56]) are shown in Fig. S 4 and reported in Supplementary Table 1. Reference-glass values agree with accepted values. Where required, an inter-sequence

excess variance was propagated into our analyses to account for minimal heterogeneity of reference glasses between the varied analytical runs (up to 10%).

- **Statistical analysis of the Sr-isotope dataset**

Measured $^{87}Sr/^{86}Sr$ obtained on Weltevreden melt inclusions show a range of values that correspond to a MSWD of 2.3. Considering the number of individual datapoints—n=137—this MSWD value translates to a $p(\chi^2)$ of 4.4×10^{-16}, i.e., largely below the accepted threshold of 5% typically used in geoscience to indicate homogeneity of a sample population[57]. This significant heterogeneity is also clearly observed for $(^{87}Sr/^{86}Sr)_{initial}$ values that show a MSWD of 2.2 translating to a $p(\chi^2)$ of 9.8×10^{-14}. Further, it is also clear from Fig. S 6 that the range of $(^{87}Sr/^{86}Sr)_{initial}$ values is not resulting from under/over correction of the $(^{87}Sr/^{86}Sr)_{measured}$ values: the range of $^{87}Rb/^{86}Sr$ is rather narrow and all analyses with elevated $^{87}Rb/^{86}Sr$, i.e. > $(^{87}Rb/^{86}Sr)_{KL2\text{-}G}$, were rejected from the dataset, preventing inaccurate over correction of $(^{87}Sr/^{86}Sr)_{measured}$. Further, since all potential sources of uncertainty have been examined and propagated in isotopic ratios, this range of $(^{87}Sr/^{86}Sr)_{initial}$ values is interpreted to reflect Sr-isotope heterogeneity of the melts that were trapped in Weltevreden olivine crystals. The observed heterogeneity in elemental and isotopic compositions in Weltevreden melt inclusions is not a unique feature since a multitude of melt inclusion studies have reported similar observations[16,18,58] for different radiogenic isotope systems, regardless of the analytical protocol (laser ablation, ion probe or thermal ionization mass spectrometry).

Hence, we can discriminate statistically homogeneous populations in this dataset. One way to achieve this is to isolate individual analyses that are in the tails of this distribution: those with $(^{87}Sr/^{86}Sr)_{initial}$ significantly–i.e., considering individual uncertainties (±2se)–outside the 95% confidence interval around the weighted mean of the dataset. Doing so yields three homogeneous populations of melt inclusions: (i) one with low $(^{87}Sr/^{86}Sr)_{initial}=0.69932\pm0.00024$ (c.i. 95%)

comprised of 14 inclusions (MSWD = 0.88, $p(\chi^2) = 0.57$), (ii) one with intermediate
608 $(^{87}Sr/^{86}Sr)_{initial}$=0.700624±0.000086 made of 116 inclusions (MSWD = 1.1, $p(\chi^2) = 0.27$) and one with elevated $(^{87}Sr/^{86}Sr)_{initial}$=0.70177±0.00024 made of 7 inclusions (MSWD = 0.48, $p(\chi^2) =$
610 0.82).

Applying of the t-test for independent populations with unequal variances[59] reveals that the
612 means of $(^{87}Sr/^{86}Sr)_{initial}$ of all groups are different with the confidence over 99.9% (see Supplementary Table 6a,b).

614 • **Model age calculation**

Sr model age of olivine-hosted melt inclusions was based on (i) $(^{87}Sr/^{86}Sr)_{initial}$ and (ii) Bulk
616 Silicate Earth (BSE) evolution. The latter is defined as follows: initial $^{87}Sr/^{86}Sr = 0.698990$ at 4.567 Ma age[60], initial BSE Rb/Sr=0.03[27] and ^{87}Rb decay constant of 1.3972×10^{-11} yr^{-1} . Even
618 considering a 15% uncertainty in the BSE Rb/Sr value Sr-model ages remain far within uncertainty of our estimates. Calculation was conducted assuming no Rb left in the BSE source
620 after melt extraction. This assumption is quite realistic since (i) degree of mantle melting is high in the hot early Earth and (ii) Rb is highly incompatible during melting. Samarium–Neodymium
622 (Sm–Nd) and Lutetium–Hafnium (Lu–Hf) model ages presented in Fig. S 2 were calculated using Ryan Ickert's spreadsheet[61].

624 • **Contamination of Weltevreden komatiites**

Studied inclusions in olivine yield significant intercorrelated variation of Cl, K, Rb, H_2O, Pb, Sr
626 and Na, which is unrelated to olivine crystallization and extraction from the melt. This is well demonstrated by the strong correlation between ratios of elements excluded from olivine
628 structure, e.g. Cl, K, Rb, H_2O, Pb, Sr, Na, and Ti, which must stay constant during olivine fractionation (Fig. S 3). Similar variations are common for submarine glasses of OIB and MORB

(Fig. S 3) and have been explained by minor (less than 1 wt%) contamination of seawater-derived ultra-saline brines[25,26]. The same explanation is also well suited for Weltevreden melt inclusions. The maximum amount of brine with a concentration of Cl of 10-30 wt% required to explain the addition of ca 0.20wt% of Cl to Weltevreden melt is about or less than 2wt%. This amount will not affect major element concentrations considering their analytical errors, but is enough to be observed in trace elements and H_2O contents. Also note that the extent of contamination tends to increase with decreasing host olivine Fo content (Figure 2c , Fig. S 3). The initial $^{87}Sr/^{86}Sr$ isotope ratio of melt inclusions does not correlate with contamination proxies (see Figure 2h); thus, we conclude that the effect of such small amounts of assimilated brine is within the analytical errors of $^{87}Sr/^{86}Sr$ determination.

Methods for numerical investigation

- **Geodynamic models: essentials and setup**

We study the thermochemical evolution of compressible mantle using the code StagYY[41], which has been developed and widely used over several decades for global-scale modelling of Earth's evolution spanning its age[11,43-45]. The model includes pressure- and temperature-dependent viscosity, plastic yielding, time-dependent radiogenic heating, core cooling and phase changes. Following a two-step mantle differentiation and utilizing water-dependent solidi functions[43], the code forms basaltic and felsic melts and considers both intrusive (plutonic) and eruptive (volcanic) magmatism[43]. The mass ratio of erupted to intruded material follows a specified constant value of 30:70 (corresponding to 30% eruption efficiency), which has been previously shown to be important for producing Archean TTG rocks[43,58,62]. We employ temperature- and pressure- dependent solubility maps for different mantle minerals, which control the water in-gassing and out-gassing[11].

We use a two-dimensional quadrant spherical annulus geometry[42] with a Eulerian mesh, whose resolution varies radially, and is higher at the core-mantle boundary, 660 km phase transition and at the surface. The computational domain consists of 512 (lateral) times 128 (radial) cells and ~ 1.3 million Lagrangian tracers carrying various quantities (temperature, composition, water content, isotopes, trace elements, etc.) are advected through it. Free slip boundary conditions are used at the core mantle boundary and at the surface. Side boundary conditions are periodic.

A visco-plastic rheology is considered where the viscous deformation is accommodated by grain-size independent diffusion creep. The mantle is divided into 3 different layers *i*: upper mantle (1), lower mantle (2) and post-perovskite layer (3), with each layer having different values for activation energy E_i and activation volume V_i[63,64]. Following the Arrhenius law, the diffusion and dislocation creep (proxy) components of the temperature- and pressure-dependent viscosity are given as:

$$\eta(T,P) = \eta_0 \Delta\eta_i \exp\left(\frac{E_i + PV(P)}{RT} - \frac{E_i}{RT_0}\right) \quad (1)$$

where η_0 is the reference viscosity ($2.35\ 10^{19}\ Pa\ s$) at zero pressure and reference temperature T_0 (1710 K), $\Delta\eta_i$ is the viscosity offset between layer *i* and the reference viscosity, *P* is the pressure, *R* is the gas constant and *T* is the absolute temperature. The activation volume decreases exponentially with increasing pressure in each layer *i* according to the relation:

$$V(P) = V_i \exp\left(-\frac{P}{P_i}\right) \quad (2)$$

where P_i is the pressure scale, which is different for each layer *i*. Plastic deformation in the lithosphere is accommodated by assuming plastic yielding[47,65]. The maximum stress that a material can sustain before deforming plastically is given by the yield stress σ_Y, which has both brittle and ductile components:

$$\sigma_Y = \min\left(\sigma_{Y,ductile}, \sigma_{Y,brittle}\right). \quad (3)$$

The ductile yield stress $\sigma_{Y,ductile}$ increases linearly with pressure as:

$$\sigma_{Y,ductile} = \sigma_Y^0 + \acute{\sigma_Y} P, \quad (4)$$

where σ_Y^0 is the surface ductile yield stress and $\acute{\sigma_Y}$ is the pressure gradient of the ductile yield stress. The brittle yield stress $\sigma_{Y,brittle}$ is calculated following the Byerlee approach as:

$$\sigma_{Y,brittle} = c + \mu P, \quad (5)$$

where c is the surface cohesion and μ is the friction coefficient. If the convective stresses exceed the yield stress, the viscosity is reduced to the yielding viscosity $\eta_Y = \sigma_Y / 2\dot{\epsilon}$, where $\dot{\epsilon}$ is the 2nd invariant of the strain-rate tensor.

See Supplementary Table 7 for model parameters used in this study. The model uses a parameterisation based on mineral physics data[66,67], in which the mantle minerals are divided into olivine (ol), pyroxene-garnet (px-gt), TTG (tonalite-trondhjemite-granodiorite), and melt phase systems. Solid-solid phase transitions are assumed (see Supplementary Table 8) and the mantle is initialised with a pyrolytic composition: 80% harzburgite and 20% basalt, being a mixture of 60% olivine and 40% pyroxene-garnet. The adiabatic temperature, density, thermal conductivity, thermal expansivity and heat capacity are pressure-dependent following a third-order Birch–Murnaghan equation of state. Further details of the model can be found in[11]. Here, we describe only the model modifications introduced in this study.

- **Geodynamic models: modifications**

1. Rheology: We improved our rheological model by adding a proxy for the pressure-, temperature- and stress-dependent dislocation creep rheology assuming stress corresponding to a geological strain rate of 10^{-15} 1/s and using dry olivine rheology parameters[68] (Supplementary Table 7). We also considered frictional plasticity with the

coefficient of friction of 0.1 corresponding to the properties of subduction channels, which lack continental sediments[46]. Similar effective friction coefficient was suggested based on the model of thermal cracking of oceanic lithosphere on early Earth[69].

1. Water solubility maps: We modified water solubility map for px-garnet phases to better fit the map calculated by Perple_X (see Fig S8).
2. Water in-gassing: In this study, we assume that at every time-step, the mantle minerals only in the top 5 km of the computational domain (as opposed to 10 km done previously) are partially saturated with water in accordance with their pressure- and temperature-dependent solubility maps with water saturation fraction α_w parameter ($0< \alpha_w <1$) controlling the input of the surface water into the lithosphere.
3. Density: We corrected density of felsic material (TTG) by considering phase transformations of feldspars and quartz at high pressures (see Fig. S 9). We have also slightly modified density changes of olivine and pyroxene-garnet compositions at phase boundaries to decrease density difference between pyrolite and pyroxene-garnet in lowermost mantle to 1.7 %, simultaneously fitting density-depth distribution in PREM model along 1600K adiabatic geotherm. We introduced the effect of water on density using a simplified relation

$$\rho_\omega = \rho_d(1 - aC_{H2O}), \quad (6)$$

where ρ_ω, ρ_d are densities of water-containing and dry material respectively, C_{H2O} is the concentration of water in weight fraction and a is a constant, typically between 1 and 2 estimated using Gibbs energy minimization code[70] (see Fig. S 9) that we consider as 2.0 in this study.
4. Conditions for felsic crust (TTG) formation from hydrated basalt: In the present study, we assume that TTG can only be produced from basalt if the latter's water content is above 0.5

wt.% (instead of 0.05 wt.% used in earlier studies) and that maximum degree of melting of basalt to produce TTG is 30% instead of 10% used in previous studies[11,43].

5. Isotopic systems and trace elements: We have introduced the evolution of Rb-Sr isotope system as well as Nb, U, Ce and Pb trace elements. Constant parameters and solid-melt partition coefficients used in the study are presented in Supplementary Tables 9, 10 respectively.

- **Geodynamic models: definition of sampling for Figures 7,8 (main text)**

For the models presented in Figures 7 and 8 (main text), we show the evolution of the mean Nb/U and Ce/Pb ratios with time for a selection of the model's cells fulfilling the following conditions: (i) Average cell temperature has to be more than 100K higher than average temperature of all cells located at the same depth. This condition allows us to identify mantle plume material. In practice, potential temperature of all selected cells in most of the models appear to be higher than 1700°C. (ii) Cells have to be located within the depth range of 400-600km. This condition is required to avoid cells from the top 300 km, from which the melt is extracted and trace elements are partitioned. (iii) Average initial Sr isotope ratio ($^{87}Sr/^{86}Sr$) of each cell has to be less than 0.6997 to identify the Hadean fraction. Following this procedure, we obtain mean values of trace elements ratios in the Hadean fraction of the potential komatiite source and standard deviations of mean values at every output model time. To avoid unrepresentative and too uncertain values, we further filter out values at times with too few Hadean cells (<=20), with too large value of 2 standard deviation of mean Nb/U ratio (>=4) and with too large 2 standard deviation of mean Ce/Pb ratio (>=2). As a result, we obtain mean values of trace element ratios and their standard deviations (multiplied by 2) for each model at every model output time, which we show in Figure 7& 8 (main text).

Due to inherent randomness of convection processes arising from the initial thermal perturbations and initial tracer positions, the model results vary even with the exact same parameters. Group I presented in Figure 7 comprises of two sets of models (3 in each set) with the same frictional strength (f=0.1) but with different water saturation fraction (alpha=0.25 or 0.20). The higher the value of alpha, the higher is the input of water into the lithosphere. Group II presented in Figure 8 also comprises of two sets of models (2 in each set) with the same frictional strength (f=0.2) but with different water saturation fraction (alpha=0.40 or 0.30). Values of alpha were chosen such that all models of both groups produce similar amount of continental crust during the Hadean.

- **Geodynamic models: parameter sensitivity**

In the main text we show the effect of lithospheric hydration and strength on the evolution of the trace elements ratios of the Hadean fraction of potential komatiite source (Figure 7). Here, we additionally show the influence of the variation of the parameter "*a*" (eq. 6) responsible for decreasing the density of rocks due to water-containing minerals. Panels a-h in Figure S10 show our models that fit well with the geochemical observations computed with our preferred value of "*a*" of 2. Panels i-p in Figure S10 show modelling results obtained with the value of "*a*" parameter of 1.5, which is more suitable for rocks at relatively high pressures (see Figure S9b) with all the other parameters same as in the models with *a*=2. As we see from Figure S10, the variation of "*a*" parameter does not change significantly the modeling results.

Acknowledgements:

We thank A. H. Wilson and G.R. Byerly for their help in fieldwork in Barberton Greenstone Belt, South Africa in 2015, and Axel Hofmann and M. Elburg in 2022. M.V. Portnyagin for providing reference glasses for calibration of Raman H_2O analysis. F. Brunet, B. Lanson, P. Roux and the direction of University Grenoble Alpes provided invaluable help in establishing and maintaining the ISTerre Micro-Analytical Platform (IMAP).

Funding:

This project is supported by a grant of the European Research Council (ERC) under the European Union's Horizon H2020 research and innovation program (Synergy Grant MEET, grant agreement no.856555) to A.V.S, S.V.S and J.W.V. ISTerre is part of the Laboratoires d'Excellence (LabEx) OSUG@2020 (ANR10 LABX56). Participation of E.V.A. and A.N.K and annealing of melt inclusions was supported by grant of Russian Research Foundation no 22-77-00081 to E.V.A. The computing time for geodynamic modelling (project bbk00014) was provided by the administration of the high-performance computer cluster "Lise" at the NHR Centre NHR@ZIB jointly supported by the Federal Ministry of Education and Research and the state government.

Author contributions:

A.V. participated in samples collection, developed the protocol for Rb-Sr isotope analyses and LA-ICP-MS Rb–Sr/TE split stream analytical mode, conducted analyses, processed Rb-Sr isotopes data, interpretated geochemical data and wrote most of the manuscript text; A.V.C. participated in samples collection, found and prepared all melt inclusions and host minerals for analytical work, conducted EPMA and Raman analyses, processed trace elements data and

participated in geochemical data interpretation; A.V.S. conceived the idea and designed the project, assisted on the collection of samples and played leading role in interpreting geochemical data; C.J. developed the geodynamic models, wrote and modified code and performed computing; S.V.S. conceived the idea and designed the geodynamic model, played leading role in interpreting and visualising results of geodynamic models and wrote most part of geodynamic modeling section; E.V.A. performed inclusions homogenization, and assisted in the collection of samples; A.N.K performed inclusions homogenization;V.G.B. developed analytical protocols for EPMA and LA-ICP-MS analyses of melt inclusions and host olivines; N.T.A. governed in the collection of samples and shared his experience in the study of komatiites; L.V.D. directed the tuning of RESolution SE laser and Agilent 8900 ICP-MS and participated in preparation of LA-ICP-MS analytical protocols; J.W.V. participated in the design of the project. All co-authors contributed to discussing and interpreting data and writing the manuscript.

Competing interests

Authors declare that they have no competing interests

References

1 O'Neil, J., Carlson, R. W., Francis, D. & Stevenson, R. K. Neodymium-142 Evidence for Hadean Mafic Crust. *Science* **321**, 1828-1831 (2008). https://doi.org:https://doi.org/10.1126/science.1161925

2 Bowring, S. A. & Williams, I. S. Priscoan (4.00–4.03 Ga) orthogneisses from northwestern Canada. *Contrib. Mineral. Petrol.* **134**, 3-16 (1999). https://doi.org:https://doi.org/10.1007/s004100050465

3 Korenaga, J. Crustal evolution and mantle dynamics through Earth history. *Philosophical Transactions of the Royal Society A: Mathematical, Physical and Engineering Sciences* **376**, 20170408 (2018). https://doi.org:https://doi.org/10.1098/rsta.2017.0408

4 Campbell, I. H. Constraints on continental growth models from Nb/U ratios in the 3.5 Ga Barberton and other Archaean basalt-komatiite suites. *Am. J. Sci.* **303**, 319-351 (2003). https://doi.org:https://doi.org/10.2475/ajs.303.4.319

5 Dhuime, B., Hawkesworth, C. J., Cawood, P. A. & Storey, C. D. A change in the geodynamics of continental growth 3 billion years ago. *Science* **335**, 1334-1336 (2012). https://doi.org:https://doi.org/10.1126/science.1216066

6 Rosas, J. C. & Korenaga, J. Rapid crustal growth and efficient crustal recycling in the early Earth: Implications for Hadean and Archean geodynamics. *EPSL* **494**, 42-49 (2018). https://doi.org:https://doi.org/10.1016/j.epsl.2018.04.051

7 McCoy-West, A. J. *et al.* Extensive crustal extraction in Earth's early history inferred from molybdenum isotopes. *Nat. Geosci.* **12**, 946-951 (2019). https://doi.org:https://doi.org/10.1038/s41561-019-0451-2

8 Hofmann, A., Class, C. & Goldstein, S. Size and composition of the MORB+ OIB mantle reservoir. *Geochem. Geophys. Geosyst.* **23** (2022). https://doi.org:https://doi.org/10.1029/2022GC010339

9 Vezinet, A., Pearson, D. G. & Thomassot, E. Effects of contamination on whole-rock isochrons in ancient rocks: a numerical modelling approach. *Lithos* **386-387**, 106040 (2021). https://doi.org:https://doi.org/10.1016/j.lithos.2021.106040

10 Whitehouse, M. Granulite fades Nd-isotopic homogenization in the Lewisian complex of northwest Scotland. *Nature* **331**, 705-707 (1988).

11 Jain, C., Rozel, A. B., van Hunen, J., Chin, E. J. & Manjón-Cabeza Córdoba, A. Building archean cratonic roots. *Frontiers in Earth Science* **10**, 966397 (2022). https://doi.org:https://doi.org/10.3389/feart.2022.966397

12 Lourenço, D. L., Rozel, A. B., Ballmer, M. D. & Tackley, P. J. Plutonic-squishy lid: A new global tectonic regime generated by intrusive magmatism on Earth-like planets. *Geochem. Geophys. Geosyst.* **21**, e2019GC008756 (2020). https://doi.org:https://doi.org/10.1029/2019GC008756

13 Hofmann, A. W., Jochum, K. P., Seufert, M. & White, W. M. Nb and Pb in oceanic basalts: new constraints on mantle evolution. *EPSL* **79**, 33-45 (1986). https://doi.org:https://doi.org/10.1016/0012-821X(86)90038-5

14 Reimink, J., Davies, J., Moyen, J. & Pearson, D. A whole-lithosphere view of continental growth. *Geochemical Perspectives Letters* **26**, 45-49 (2023). https://doi.org:https://doi.org/10.7185/geochemlet.2324

15 Sobolev, A. V. *et al.* Deep hydrous mantle reservoir provides evidence for crustal recycling before 3.3 billion years ago. *Nature* **571**, 555-559 (2019). https://doi.org:https://doi.org/10.1038/s41586-019-1399-5

16 Sobolev, A. V., Hofmann, A. W., Jochum, K. P., Kuzmin, D. V. & Stoll, B. A young source for the Hawaiian plume. *Nature* **476**, 434-437 (2011). https://doi.org:https://doi.org/10.1038/nature10321

17 Sobolev, A. V. *et al.* Komatiites reveal a hydrous Archaean deep-mantle reservoir. *Nature* **531**, 628-632 (2016). https://doi.org:https://doi.org/10.1038/nature17152

18 Saal, A., Hart, S., Shimizu, N., Hauri, E. & Layne, G. Pb isotopic variability in melt inclusions from oceanic island basalts, Polynesia. *Science* **282**, 1481-1484 (1998). https://doi.org:https://doi.org/10.1126/science.282.5393.1481

19 Jackson, M. G. & Hart, S. R. Strontium isotopes in melt inclusions from Samoan basalts: Implications for heterogeneity in the Samoan plume. *EPSL* **245**, 260-277 (2006). https://doi.org:https://doi.org/10.1016/j.epsl.2006.02.040

20 McDonough, W. & Ireland, T. Intraplate origin of komatiites inferred from trace elements in glass inclusions. *Nature* **365**, 432-434 (1993). https://doi.org:https://doi.org/10.1038/365432a0

21 Connolly, B. D. *et al.* Highly siderophile element systematics of the 3.3 Ga Weltevreden komatiites, South Africa: implications for early Earth history. *EPSL* **311**, 253-263 (2011). https://doi.org:https://doi.org/10.1016/j.epsl.2011.09.039

22 Hofmann, A., Anhaeusser, C. & Li, X. Layered ultramafic complexes of the Barberton Greenstone Belt–age constraints and tectonic implications. *S. Afr. J. Geol.* **124**, 7-16 (2021). https://doi.org:https://doi.org/10.25131/sajg.124.0002

23 Puchtel, I. *et al.* Insights into early Earth from Barberton komatiites: evidence from lithophile isotope and trace element systematics. *Geochim. Cosmochim. Acta* **108**, 63-90 (2013). https://doi.org:https://doi.org/10.1016/j.gca.2013.01.016

24 Roerdink, D. L., Ronen, Y., Strauss, H. & Mason, P. R. Emergence of felsic crust and subaerial weathering recorded in Palaeoarchaean barite. *Nat. Geosci.* **15**, 227-232 (2022). https://doi.org:https://doi.org/10.1038/s41561-022-00902-9

25 Coombs, M. L., Sisson, T. W. & Kimura, J.-I. Ultra-high chlorine in submarine Kılauea glasses: evidence for direct assimilation of brine by magma. *EPSL* **217**, 297-313 (2004). https://doi.org:https://doi.org/10.1016/S0012-821X(03)00631-9

26 Kendrick, M. A., Arculus, R., Burnard, P. & Honda, M. Quantifying brine assimilation by submarine magmas: Examples from the Galápagos Spreading Centre and Lau Basin. *Geochim. Cosmochim. Acta* **123**, 150-165 (2013). https://doi.org:https://doi.org/10.1016/j.gca.2013.09.012

27 McDonough, W. F. & Sun, S.-s. The composition of the Earth. *Chem. Geol.* **120**, 223-253 (1995). https://doi.org:https://doi.org/10.1016/0009-2541(94)00140-4

28 Hofmann, A. W. Chemical differentiation of the Earth: the relationship between mantle, continental crust, and oceanic crust. *EPSL* **90**, 297-314 (1988). https://doi.org:https://doi.org/10.1016/0012-821X(88)90132-X

29 Lyubetskaya, T. & Korenaga, J. Chemical composition of Earth's primitive mantle and its variance: 1. Method and results. *Journal of Geophysical Research: Solid Earth* **112** (2007). https://doi.org:https://doi.org/10.1029/2005JB004223

30 Puchtel, I. S., Blichert-Toft, J., Horan, M. F., Touboul, M. & Walker, R. J. The komatiite testimony to ancient mantle heterogeneity. *Chem. Geol.* **594**, 120776 (2022). https://doi.org:https://doi.org/10.1016/j.chemgeo.2022.120776

31 Corgne, A., Liebske, C., Wood, B. J., Rubie, D. C. & Frost, D. J. Silicate perovskite-melt partitioning of trace elements and geochemical signature of a deep perovskitic reservoir.

Geochim. Cosmochim. Acta **69**, 485-496 (2005). https://doi.org:https://doi.org/10.1016/j.gca.2004.06.041

32 Tilhac, R., Begg, G. C., O'Reilly, S. Y. & Griffin, W. L. A global review of Hf-Nd isotopes: New perspectives on the chicken-and-egg problem of ancient mantle signatures. *Chem. Geol.* **609**, 121039 (2022). https://doi.org:https://doi.org/10.1016/j.chemgeo.2022.121039

33 Wedepohl, K. H. The composition of the continental crust. *Geochim. Cosmochim. Acta* **59**, 1217-1232 (1995).

34 Rudnick, R. L. & Fountain, D. M. Nature and composition of the continental crust: a lower crustal perspective. *Rev. Geophys.* **33**, 267-309 (1995). https://doi.org:https://doi.org/10.1029/95RG01302

35 Taylor, S. R. & McLennan, S. M. *The continental crust: its composition and evolution*. (Blackwell Scientific Publications, 1985).

36 McLennan, S. M. Relationships between the trace element composition of sedimentary rocks and upper continental crust. *Geochem. Geophys. Geosyst.* **2** (2001). https://doi.org:https://doi.org/10.1029/2000GC000109

37 Armstrong, R. L. Radiogenic isotopes: the case for crustal recycling on a near-steady-state no-continental-growth Earth. *Phil. Trans. R. Soc. London, Ser. A* **301**, 443-472 (1981). https://doi.org:https://doi.org/10.1098/rsta.1981.0122

38 Harrison, T. M. *Hadean Earth*. (Springer Cham, 2020).

39 Bauer, A. *et al.* Hafnium isotopes in zircons document the gradual onset of mobile-lid tectonics. *Geochemical Perspectives Letters* **14**, 1-6 (2020). https://doi.org:https://doi.org/10.7185/geochemlet.2015

40 Tusch, J. *et al.* Long-term preservation of Hadean protocrust in Earth's mantle. *Proceedings of the National Academy of Sciences* **119** (2022). https://doi.org:https://doi.org/10.1073/pnas.2120241119

41 Tackley, P. J. Modelling compressible mantle convection with large viscosity contrasts in a three-dimensional spherical shell using the yin-yang grid. *Phys. Earth Planet. Inter.* **171**, 7-18 (2008). https://doi.org:https://doi.org/10.1016/j.pepi.2008.08.005

42 Hernlund, J. W. & Tackley, P. J. Modeling mantle convection in the spherical annulus. *Phys. Earth Planet. Inter.* **171**, 48-54 (2008). https://doi.org:https://doi.org/10.1016/j.pepi.2008.07.037

43 Jain, C., Rozel, A. B., Tackley, P. J., Sanan, P. & Gerya, T. V. Growing primordial continental crust self-consistently in global mantle convection models. *Gondwana Res.* **73**, 96-122 (2019). https://doi.org:https://doi.org/10.1016/j.gr.2019.03.015

44 Xie, S. & Tackley, P. J. Evolution of helium and argon isotopes in a convecting mantle. *Phys. Earth Planet. Inter.* **146**, 417-439 (2004). https://doi.org:https://doi.org/10.1016/j.pepi.2004.04.003

45 Xie, S. & Tackley, P. J. Evolution of U-Pb and Sm-Nd systems in numerical models of mantle convection and plate tectonics. *Journal of Geophysical Research: Solid Earth* **109** (2004). https://doi.org:https://doi.org/10.1029/2004JB003176

46 Sobolev, S. V. & Brown, M. Surface erosion events controlled the evolution of plate tectonics on Earth. *Nature* **570**, 52-57 (2019). https://doi.org:https://doi.org/10.1038/s41586-019-1258-4

47 Tackley, P. J. Self-consistent generation of tectonic plates in time-dependent, three-dimensional mantle convection simulations. *Geochem. Geophys. Geosyst.* **1** (2000). https://doi.org:https://doi.org/10.1029/2000GC000036

48 Danyushevsky, L. V. & Plechov, P. Petrolog3: Integrated software for modeling crystallization processes. *Geochem. Geophys. Geosyst.* **12** (2011). https://doi.org:https://doi.org/10.1029/2011GC003516

49 Kazzy, C. *et al.* Study of olivine-hosted melt and spinel inclusions from the Song Da ultramafic volcanic suite, northern Vietnam: Compositions, crystallization temperatures, and origin of the low-Ti komatiite-like and high-Ti primary melts. *Chem. Geol.*, 122219 (2024). https://doi.org:https://doi.org/10.1016/j.chemgeo.2024.122219

50 Falloon, T. J. & Danyushevsky, L. V. Melting of refractory mantle at 1· 5, 2 and 2· 5 GPa under anhydrous and H2O-undersaturated conditions: implications for the petrogenesis of high-Ca boninites and the influence of subduction components on mantle melting. *J. Petrol.* **41**, 257-283 (2000). https://doi.org:https://doi.org/10.1093/petrology/41.2.257

51 Koornneef, J. M. *et al.* TIMS analysis of Sr and Nd isotopes in melt inclusions from Italian potassium-rich lavas using prototype 1013 Ω amplifiers. *Chem. Geol.* **397**, 14-23 (2015). https://doi.org:https://doi.org/10.1016/j.chemgeo.2015.01.005

52 Paton, C., Hellstrom, J., Paul, B., Woodhead, J. & Hergt, J. Iolite: Freeware for the visualisation and processing of mass spectrometric data. *J. Anal. At. Spectrom.* **26**, 2508-2518 (2011). https://doi.org:https://doi.org/10.1039/C1JA10172B

53 Currie, L. A. Limits for qualitative detection and quantitative determination. Application to radiochemistry. *Analytical chemistry* **40**, 586-593 (1968).

54 Horstwood, M. S. *et al.* Community-Derived Standards for LA-ICP-MS U-(Th-)Pb Geochronology–Uncertainty Propagation, Age Interpretation and Data Reporting. *Geostand. Geoanal. Res.* **40**, 311-332 (2016). https://doi.org:https://doi.org/10.1111/j.1751-908X.2016.00379.x

55 Jochum, K. P. *et al.* MPI-DING reference glasses for in situ microanalysis: New reference values for element concentrations and isotope ratios. *Geochem. Geophys. Geosyst.* **7** (2006). https://doi.org:https://doi.org/10.1029/2005GC001060

56 Jochum, K. P. *et al.* Determination of reference values for NIST SRM 610–617 glasses following ISO guidelines. *Geostand. Geoanal. Res.* **35**, 397-429 (2011). https://doi.org:https://doi.org/10.1111/j.1751-908X.2011.00120.x

57 Wendt, I. & Carl, C. The statistical distribution of the mean squared weighted deviation. *Chemical Geology: Isotope Geoscience Section* **86**, 275-285 (1991). https://doi.org:https://doi.org/10.1016/0168-9622(91)90010-T

58 Reinhard, A. *et al.* Sr and Nd isotopic compositions of individual olivine-hosted melt inclusions from Hawai'i and Samoa: Implications for the origin of isotopic heterogeneity in melt inclusions from OIB lavas. *Chem. Geol.* **495**, 36-49 (2018). https://doi.org:https://doi.org/10.1016/j.chemgeo.2018.07.034

59 Welch, B. L. The generalization of 'STUDENT'S'problem when several different population varlances are involved. *Biometrika* **34**, 28-35 (1947). https://doi.org:https://doi.org/10.1093/biomet/34.1-2.28

60 Wasserburg, G., Papanastassiou, D. & Sanz, H. Initial strontium for a chondrite and the determination of a metamorphism or formation interval. *EPSL* **7**, 33-43 (1969). https://doi.org:https://doi.org/10.1016/0012-821X(69)90008-9

61 Ickert, R. B. Algorithms for estimating uncertainties in initial radiogenic isotope ratios and model ages. *Chem. Geol.* **340**, 131-138 (2013). https://doi.org:https://doi.org/10.1016/j.chemgeo.2013.01.001

62 Rozel, A., Golabek, G. J., Jain, C., Tackley, P. J. & Gerya, T. Continental crust formation on early Earth controlled by intrusive magmatism. *Nature* **545**, 332-335 (2017). https://doi.org:https://doi.org/10.1038/nature22042

63 Karato, S.-i. & Wu, P. Rheology of the upper mantle: A synthesis. *Science* **260**, 771-778 (1993). https://doi.org:https://doi.org/10.1126/science.260.5109.771

64 Yamazaki, D. & Karato, S.-I. Some mineral physics constraints on the rheology and geothermal structure of Earth's lower mantle. *Am. Mineral.* **86**, 385-391 (2001). https://doi.org:https://doi.org/10.2138/am-2001-0401

65 Moresi, L. & Solomatov, V. Mantle convection with a brittle lithosphere: thoughts on the global tectonic styles of the Earth and Venus. *Geophys. J. Int.* **133**, 669-682 (1998). https://doi.org:https://doi.org/10.1046/j.1365-246X.1998.00521.x

66 Irifune, T. & Ringwood, A. Phase transformations in subducted oceanic crust and buoyancy relationships at depths of 600–800 km in the mantle. *EPSL* **117**, 101-110 (1993). https://doi.org:https://doi.org/10.1016/0012-821X(93)90120-X

67 Ono, S., Ito, E. & Katsura, T. Mineralogy of subducted basaltic crust (MORB) from 25 to 37 GPa, and chemical heterogeneity of the lower mantle. *EPSL* **190**, 57-63 (2001). https://doi.org:https://doi.org/10.1016/S0012-821X(01)00375-2

68 Hirth, G. & Kohlstedf, D. in *Inside the Subduction Factory* Vol. 138 *Geophysical monograph-American Geophysical Union* 83-106 (2003).

69 Korenaga, J. Thermal cracking and the deep hydration of oceanic lithosphere: A key to the generation of plate tectonics? *Journal of Geophysical Research: Solid Earth* **112** (2007). https://doi.org:https://doi.org/10.1029/2006JB004502

70 Sobolev, S. V. & Babeyko, A. Y. Modeling of mineralogical composition, density and elastic wave velocities in anhydrous magmatic rocks. *Surv. Geophys.* **15**, 515-544 (1994). https://doi.org:https://doi.org/10.1007/BF00690173

Supplementary Files

This is a list of supplementary files associated with this preprint. Click to download.

- 20231120122ArticleandMethodsv0.pdf
- 20231120122ExplanatoryFileforSOMTablesv0.pdf
- ExplanatoryFileforSOMTablesv0.docx
- SOMTables.xlsx
- 20231120122TablesSOMv0.xlsx